Multi-point aerodynamic optimisation of sailplane horizontal tailplanes

A van Rooyen

21668299

Dissertation submitted in fulfilment of the requirements for the degree *Magister* in Mechanical Engineering at the Potchefstroom Campus of the North-West University

Supervisor: Dr JJ Bosman

November 2015

Abstract

A new horizontal tailplane for a high performance sailplane was developed through multi-point aerodynamic optimisation. This was achieved through the use of logged flight data, from which the operating spectrum of the horizontal tailplane of a specific sailplane was obtained.

With the operating spectrum, a modified lifting line model implementing Xfoil and the Generalised Reduced Gradient optimisation algorithm were used to optimise the aerodynamic performance of the JS1-C 21m horizontal tailplane.

Verification of the planform calculations was conducted with the commercial CFD software package Star-CCM+. The $k-\omega\ SST$ turbulence and $\gamma - Re_\theta$transition models were used for aerodynamic analysis in the verification process.

The design of new horizontal tailplane tip sections was also performed with the use of CFD. Firstly the elevator span to horizontal tailplane span ratio best suited to the operating spectrum of the horizontal tailplane was evaluated. Secondly a wingtip shape proposed by Hoerner (1965) was implemented.

The flight data-based multipoint optimisation of the planform of the horizontal tailplane shows appreciable performance increases compared to a baseline tailplane. Calculations show a 14% drag reduction for the tailplane over a sample flight. The tip design also shows a drag decrease of 1.1% at 150km/h and 3.3% drag decrease at 250km/h compared to the baseline tip section shape.

Keywords

Sailplane, Horizontal tailplane, Aerodynamic optimisation, Planform shape, Induced drag, profile drag.

Acknowledgements

First and foremost I would like to thank my Heavenly Father for the talents and strength He gave me.

Secondly I would like to thank my supervisor Dr. Johan Bosman for being an inspiration and for the support and guidance I received from him in the time of this study.

Last but not least I would like to thank my father Ronnie, my mother, Susan and other family and friends for their love and support throughout this period in the times when I needed it most.

Table of Contents

Table of Figures

List of Tables

Nomenclature

Symbol		Description
α [°]	-	Wing angle-of-attack
α_0 [°]	-	Zero lift angle of attack
α_e [°]	-	Effective angle of attack
α_H [°]	-	Horizontal tailplane angle-of-attack
α_i [°]	-	Induced angle of attack
α_W [°]	-	Induced downwash angle of the wing
AR_H [−]	-	Horizontal tailplane aspect ratio
γ [°]	-	Glide angle
c [m]	-	Chord
c_μ or $\bar{c}$ [m]	-	Wing aerodynamic chord
C_{l_α} [$1/rad$]	-	Airfoil lift curve slope
C_{l_η} [$1/rad$]	-	Airfoil elevator lift curve slope
C_{D_i} [−]	-	Induced drag coefficient
C_{d_p} [−]	-	Airfoil profile drag coefficient
C_{D_p} [−]	-	Profile drag coefficient
C_{L_H} [−]	-	Horizontal tailplane lift coefficient
C_{L_W} [−]	-	Wing lift coefficient
C_{M_0} [−]	-	Zero-lift moment coefficient of the sailplane

$C_{M_{oW}}$ $[-]$	-	Wing moment coefficient
$C_{M_{CG}}$ $[-]$	-	Moment coefficient about the centre of gravity
D $[N]$	-	Drag
$\overline{D}_i$ $[N.s]$	-	Time based induced drag
$\overline{D}_p$ $[N.s]$	-	Time-based profile drag
$\overline{D}_{iT}$ $[N.s]$	-	Total time-based induced drag for a flight
$\overline{D}_{pT}$ $[N.s]$	-	Total time-based profile drag for a flight
Δt $[s]$	-	Time spent at a flight point
δ_e or η_e [°]	-	Elevator deflection
ε [°]	-	Downwash angle
ε_H or i_H[°]	-	Horizontal tailplane incidence angle
ε_R $[-]$	-	Elevator to total horizontal tailplane span ratio
h_p $[m]$	-	Pressure altitude
i_W [°]	-	Wing incidence angle
k $[-]$	-	Gust alleviation factor
L $[N]$	-	Lift
L_H $[N]$	-	Horizontal tailplane lift
l_H or l'_H $[m]$	-	Distance between the sailplane centre of gravity and aerodynamic centre of the horizontal tailplane
L_r $[N]$	-	Radial or turn lift component

$L_S\ [N]$	-	Total sailplane lift
$L_v\ [N]$	-	Vertical lift component in banked flight
$L_W\ [N]$	-	Wing lift
$l_W\ [m]$	-	Distance between the wings aerodynamic centre and centre of gravity
$m\ [kg]$	-	Sailplane mass
$M_{0W}\ [N.m]$	-	Wing moment about its aerodynamic centre
$M_{CG}\ [N.m]$	-	Sailplane moment about its centre of gravity
$n\ [-]$	-	Load factor
$n_1\ to\ n_4\ [-]$	-	Fixed manoeuvring envelope load factors
$\eta_{MEmax}\ [°]$	-	Maximum manoeuvring envelope elevator deflection
$\eta_{GEmax}\ [°]$	-	Maximum gust envelope elevator deflection
$\mu\ [Pa.s]$	-	Dynamic viscosity
$q\ [kg/m.s]$	-	Dynamic pressure
$R\ [m]$	-	Turn radius
$R\ [-]$	-	Ratio used in Pierces criteria
$Re\ [-]$	-	Reynolds number
$\rho\ [kg/m^3]$	-	Air density
$\rho_0\ [kg/m^3]$	-	Air density at standard sea level conditions
$\sigma\ [-]$	-	Data set standard deviation
$\Psi[°]$	-	Direction indicator degrees from north

$\dot{\Psi}$ $[°/s]$	-	Turn rate
ϕ $[°]$	-	Bank angle
S_H $[m^2]$	-	Horizontal tailplane area
SM $[-]$	-	Static margin
S_V $[m^2]$	-	Vertical tailplane area
S_W $[m^2]$	-	Wing area
U $[m/s]$	-	Gust velocity
ν $[m^2/s]$	-	Kinematic viscosity
V_∞ $[m/s]$	-	Free stream velocity
V_{TAS} $[m/s]$	-	True airspeed
V_A $[m/s]$	-	Design manoeuvring speed
V_B $[m/s]$	-	Design gust speed
V_D $[m/s]$	-	Design maximum speed
V_F $[m/s]$	-	Flap design speed
V_H $[m^3/rad]$	-	Horizontal tailplane volume
$\bar{V}_H$ $[-]$	-	Horizontal tailplane volume coefficent
V_{s1} $[m/s]$	-	Wing stall speed with flaps neutral
w_i $[m/s]$	-	Downwash velocity
x_{AC} $[m]$	-	Aerodynamic centre position of the wing
x_{CG} $[m]$	-	Centre of gravity position

x_m $[-]$	-	Data set mean
x_N $[m]$	-	Neutral point position
y_i $[m]$	-	Span wise location

1. INTRODUCTION

1.1. Preface

Gliders lie deeply embedded in aviation history. The German aviation pioneer Otto Lilienthal was the first person to achieve well-documented, controlled and sustained flight with his gliders. Lillienthal was credited by the Wright brothers as a major inspiration for their decision to pursue manned flight. Gliders provided the brothers with a research platform which gave them the needed experience and data to realise their dream of powered flight.

The use of gliders didn't stop after powered flight had been achieved. Their lack of power plants, reduced complexity and cost made them especially useful as experimental aircraft. As a sport, gliding took off in the 1920s. Initially the objective was to increase the duration of flights but soon pilots began to attempt cross-country flights away from the place of launch. Improvements in aerodynamics and the understanding of weather phenomena allowed greater distances at higher average speeds.

Modern high-performance sailplanes can fly tasks exceeding 2000km with theoretical glide ratios higher than 1:70. In order to achieve this remarkable performance traditional high cost and time-consuming design methods were abandoned due to the fact that the constraints on these methods usually yielded designs which were not fully optimised.

In general aircraft design engineers optimise aircraft for a specific flight condition or a small set of conditions. Optimising an aircraft for a small set of conditions has a negative effect on overall aerodynamic efficiency due to inadequate aerodynamic performance in off design flight regimes. These trade-offs can, however, be justified when the aircraft has a set mission as in the case of large passenger aircraft where a high percentage of flight time is spent in cruise and thus at a design point. The broad operating spectrum of sailplanes, however, creates unique challenges when it comes to aerodynamic optimisation, not only due to the vast number of variables present

but also the difficulty of quantifying and setting up adequate design points and minimising the trade-offs between these points.

In March 1995 a world standard for flight recording was approved by the FIA to ensure verifiable flight recordings for badge, record and competition flights. These recordings became an important tool which enabled pilots to review flights and improve their flying abilities. Due to this an abundance of records of flights is available to sailplane designers. These recordings can serve as a valuable tool to assess and quantify the operating spectrum of sailplane configurations and thus providing the needed design points needed in the optimisation procedure. Although the multi-point optimisation of an entire sailplane may be desirable, the complexity of such a feat will drive the computational resources needed through the roof, making this approach unpractical with current computer technology.

It will thus be desirable to concentrate on a single aerodynamic component and optimise a known dominant aerodynamic feature. For this reason the planform shape of the tailplane was chosen due to its known effect on the major drag components present in a wing. The complex interaction of parameters in wing design makes the problem a prime candidate for numerical methods. These methods have been used successfully in the past to provide improvements even though the performance improvements possible have shrunk considerably in the last two decades. For this reason the improvement in overall sailplane performance can be expected to be small due to the relatively small drag contribution made by the tailplane to total sailplane drag.

1.2. Problem definition

Refinement of the major aerodynamic components of sailplanes has reached a high level of sophistication over the last two decades. Modern sailplanes consist of highly aerodynamically optimised wings, wing body connections and fuselages. With the ever-shrinking drag reduction possibilities in modern sailplane design, attention needs to be shifted to previously neglected aerodynamic components. The use of single point optimisation, however, is producing unsatisfactory results in off design flight regimes. Multi-point aerodynamic optimisation methods are thus needed to increase the aerodynamic efficiency of sailplane components over their entire operating spectrum. The drag reduction expected in multi-point optimisation of the the horizontal tailplane, will help give an advantage in the extremely competitive environment of modern gliding.

1.3. Objectives of this study

The objective of this study is the flight data-based multi-point aerodynamic optimisation of the horizontal tailplane for sailplanes. This is to be accomplished without any reductions in handling qualities and safety. The primary objective of this study can be sub-divided into the following:

- Flight analysis
- Formulation of the optimisation problem
- Method verification
- Tip section design

1.3.1. Flight analysis

In its raw form standard sailplane flight recordings contain recordings of true airspeed, pressure altitude, latitude and longitude, etc. at pre-defined time intervals. In conventional flight tests measurements of angle of attack, control surface deflections are included in the recordings. It is, however, impractical for sailplane pilots to log these measurements. The basic objective in flight analysis is thus to find the operating spectrum of the horizontal tailplane and to be able to assess design changes on the overall efficiency of the horizontal tailplane.

1.3.2. Formulation of the optimisation problem

Formulation of the optimisation problem can be sub-divided into the following objectives:

- Identification of important design variables
- Formulation of constraints to be imposed on the optimisation procedure
- Formulation of an objective function to be minimized
- Evaluation and selection of an optimisation algorithm

The formulation of an optimisation problem begins with identifying the underlying design variables, which are primarily varied during the optimisation procedure (Deb 1995). Some of these variables will be very important due to their influence on the design and are thus called the design variables. Other less important variables usually remain constant or vary in relation to the design variables. It is thus necessary to identify the important design variables of this problem.

Constraints represent functional relationships among design variables and other design parameters. To ensure design practicality some constraints should be imposed on the optimisation of the objective function. The primary function of the horizontal tailplane is longitudinal stability, the most important will be one or more constraints to ensure an optimum aerodynamic design that still conforms to stability requirements. Constraints should thus be formulated and imposed on the optimisation procedure.

Central to all optimisation problems is the objective function dependent on the design variables. Engineering objectives require either minimisation or maximisation of the objective function. In the case of this study minimisation of drag over a given operating spectrum is of importance. This function should thus be representative of all flight regimes applicable to sailplane flight.

In order to minimise the objective function an appropriate minimisation or optimisation algorithm should be selected. Numerous optimisation algorithms have been proposed and implemented in the past. Some of these have been implemented in software specifically developed to solve optimisation problems. An appropriate algorithm should thus be selected for the problem stated in this study.

1.3.3. Design verification

In the past verification of aerodynamic designs were conducted in wind tunnels. Before the advent of computers this method was used in the design and testing phase of aircraft development. The major drawback of this method is the operational cost and the amount of time needed to do these tests. The advent of computational fluid dynamic (CFD) ushered in a new era of aerodynamic design and also verification of aerodynamic ideas and designs. The objective in the design verification will be to verify the results of the optimisation procedure.

1.3.4. Tip section design

Properly designed wingtips have shown appreciable performance increases. This is usually achieved with the addition of winglets on the main wing. Other simpler wingtip geometries have also shown promise which will be suitable for the horizontal tailplane. The objective in the tip section design will be to design suitable tip geometry for a sailplane horizontal tailplane.

1.4. Layout of this dissertation

Chapter 2: Literature study, related topics will be discussed

Chapter 3: Flight analysis, explanation and discussion of the flight analysis procedure and results.

Chapter 4: Horizontal tailplane drag, selection and validation of aerodynamic models, explanation and discussion of the horizontal tailplane drag analysis procedure and results.

Chapter 5: Planform optimisation, explanation and discussion of the planform optimisation procedure and results.

Chapter 6: Tip section design, explanation and discussion of the tip section design procedure and results.

Chapter 7: Conclusions and recommendations, brief overview of this dissertation and recommendations for further study.

2. LITERATURE STUDY

2.1. Introduction

Optimisation methods can be traced back to the days of Newton, Lagrange and Cauchy. Firstly the development of differential calculus methods of optimisation was possible due to the contribution of Newton and Leibnitz to calculus. The foundations of calculus of variations, which deals with minimisation of functions, were laid by Bernoulli, Euler, Lagrange and Weirstrass. Optimisation methods for constrained problems, involving the addition of unknown multipliers, were developed by Lagrange. The first application of the steepest descent method was made by Cauchy to solve unconstrained minimisation problems. Very little progress was, however, made until the middle of the twentieth century; this was mostly due to the advent of digital computing which made the implementation of these methods possible. This produced huge advances and resulted in the emergence of several new ideas in optimisation (Rao 2009).

In aircraft design these methods are usually used to minimise the weight of structures (Rao 2009). It has become desirable to apply these methods to aerodynamic design. With the advances in computational fluid dynamics in the last three decades studies showing drag reductions of up to 8 % as in the case of the optimisation study done by Luy, Kenway and Martins on a benchmark passenger aircraft wing.

In this section numerical aerodynamic methods and previous work in applicable aerodynamic optimisation from literature are evaluated. This serves as an indication to what tools, methodologies and methods should be used in this study.

2.2. Sailplane flight

In cross-country flights sailplanes extract energy from two sources, rising columns of air called thermals and gravity in gliding flight. Where the first, thermals, are used to acquire potential energy and the latter, gravity, is used to convert the potential energy to kinetic energy. In its simplest form cross-country flight involves a series of climbs and glides from one thermal to another (Tomas & Milgram 1999). This process is repeated numerous times over the duration of a flight. Sailplane flight can thus be sub-divided into thermal or climbing flight, and the inter-thermal glide.

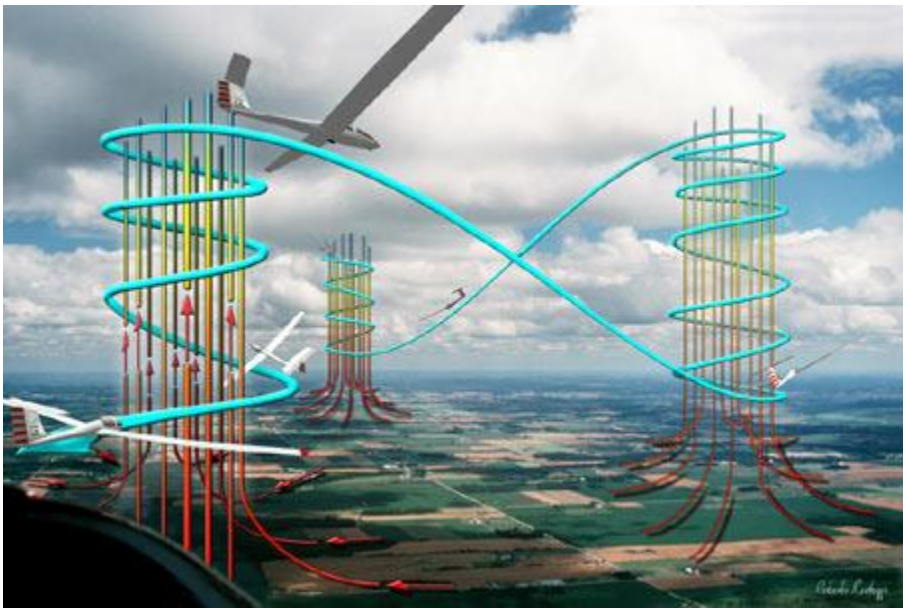

Figure 1: Usual cross-country flight path of a sailplane

In cross-country flight average cross-country speed is determined by the time required to glide from thermal exit altitude to the next thermal and to regain altitude. Average cross-country speed is thus optimised by designing the sailplane for (Tomas & Milgram 1999):

- A low sink rate while circling
- A low sink rate while gliding between thermals
- A high inter-thermal glide speed

The goal is thus to find an appropriate balance between the circling sink rate, glide angle (glide ratio) and inter-thermal glide speed. Optimising a sailplane has an

inherent difficulty due to the contradictory requirements for a high glide speed and a small glide angle.

2.2.1. Thermal flight

Thermals are spatially and localised parts of the atmosphere created by solar radiation heating the ground, typically moving upwards with a speed in the range of 1 to 10 $m.s^{-1}$ (Ákos *et al.* 2010). As altitude is always lost due to the drag of the sailplane the importance of a high lift to drag ratio can be seen here as the climb speed will be the difference between the speed of the rising air and the sink rate of the sailplane. With less time spent in thermal flight more time can be spent in inter-thermal gliding over the flight duration to increase the distance covered.

For a given thermal, the area of lift is limited and the climb must take place in continual turn. This gives thermal flight its characteristic upward spiral flight path as shown in Figure 1. From this spiral path it can be seen that the sailplane is in constant climbing, turning flight. Figure 2 shows the forces on a sailplane in thermal flight.

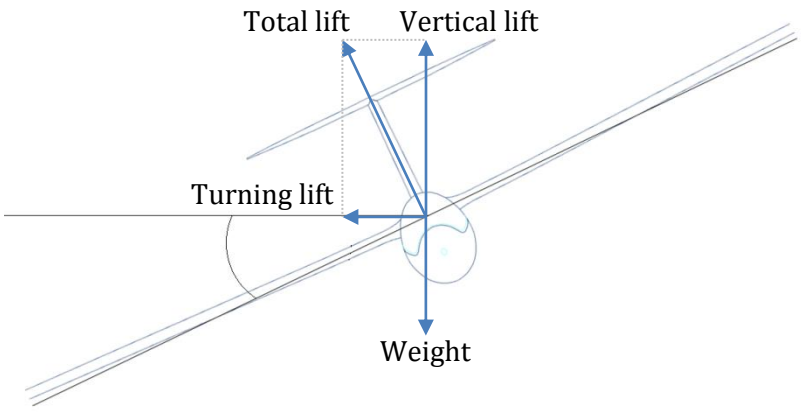

Figure 2: Forces on a sailplane in thermal flight

From Figure 2 it is seen that the total lift of the sailplane is perpendicular to its wings. The total lift can be split into two components, the component of lift needed to maintain the turn and the component needed to maintain the climb. For this

reason the sailplane takes on a banked attitude. It is due to the combination of the turning lift component and the vertical acceleration needed to climb that thermal flight is characterised by high sailplane lift coefficients. Furthermore the small turning radius needed to stay inside the lift area keeps the airspeed low due to the high rate of direction change needed in this flight condition.

2.2.2. Inter-thermal glide

In the inter-thermal glide the potential energy gained in thermal flight can be converted into kinetic energy. This increases the airspeed of the sailplane but at a cost in altitude. Again the glide ratio of the sailplane is important as this value determines the distance the sailplane can cover with the altitude gained in thermal flight. When exiting a thermal the pilot must choose the airspeed to fly to the next thermal. The inter-thermal glide speed has an appreciable influence on average cross-country speed as seen in Figure 3.

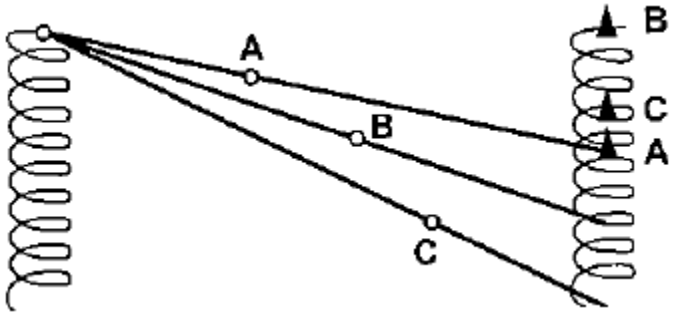

Figure 3: Optimum inter-thermal speed (Tomas & Milgram 1999)

If the pilot flies at the airspeed for the best glide angle, the sailplane will reach the next thermal with the least altitude loss as is seen in glide path A. At higher airspeed the sailplane reaches the next thermal earlier than in case A. From this it can be seen that a faster descent rate may be advantageous as the altitude lost in case B can be regained before the slower sailplane even reaches the thermal. From the pilot's point of view the basic problem remains how to get the most out of a given sailplane design. The designer, on the other hand, is interested in the impact that design variations have on overall cross-country performance.

2.2.3. Sailplane flight data logging

The IGC Data File Standard was initially developed by a group consisting of representatives of IGC, sailplane manufacturers and a number of independent software developers mainly concerned with flight data analysis programmes. After discussion and development during 1993 and 1994 it was initially defined in December 1994 and became part of official IGC/FAI documents after approval by IGC in March 1995. It has been refined and developed through regular amendments. It provides a common world standard data format for the verification of flights to FAI/IGC criteria.

Various records are added to the IGC file over the duration of a flight. The record of interest for this study is the B or Fix record. This record contains various measurements at predetermined time intervals. Of these measurements it is important that the B record should contain measurements for pressure altitude, true airspeed and a direction indicator. From these three measurements the operating spectrum of the horizontal tailplane can be calculated. Figure 4 gives a visual representation of the flight data superimposed on a map. The purple triangle shown gives the distance that will be used to calculate the average speed for points. For this reason only B records recorded between the start and end of this triangle can be used as design data.

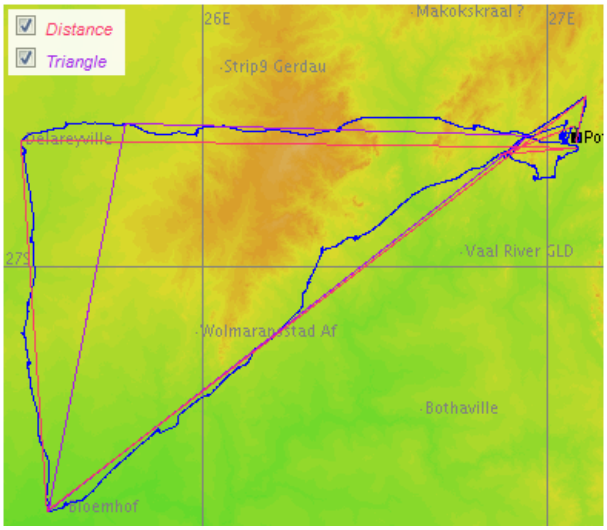

Figure 4: Visualisation of IGC file data

2.3. The horizontal tailplane

The horizontal tailplane has the task of maintaining the longitudinal stability and pitching moment equilibrium in all steady and transient flight conditions (Tomas & Milgram 1999).

2.3.1. Longitudinal dynamic stability

Dynamic longitudinal stability may be modelled mathematically as a set of linear differential equations dependant on four variables:

- Velocity
- Angle-of-attack
- Pitch angle
- Elevator deflection

Of the four solutions to this system two are of particular interest, the phugoid and short-period mode. In each case the behaviour of the aircraft depends on specific aspects of the design.

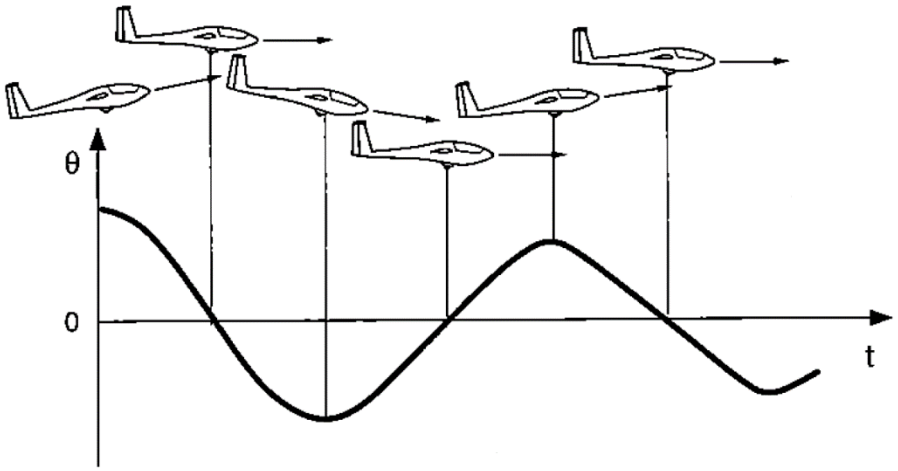

Figure 5: The phugoid mode (Tomas & Milgram 1999)

Figure 5 shows the phugoid mode. The phugoid is an oscillation involving variation of airspeed and pitch angle at constant angle-of-attack. The problem is completely defined by these two degrees of freedom, so that although altitude varies as well, it is not seen as an independent state. For small amplitude oscillations about a nominal trim condition, it can be shown that the period of oscillation is proportional to the trim airspeed and the damping inversely proportional to the lift to drag ratio of an aircraft. For this reason the phugoid is very lightly damped in modern sailplanes and may even be slightly unstable. Due to the long period, however, the pilot can control it easily with little conscious effort.

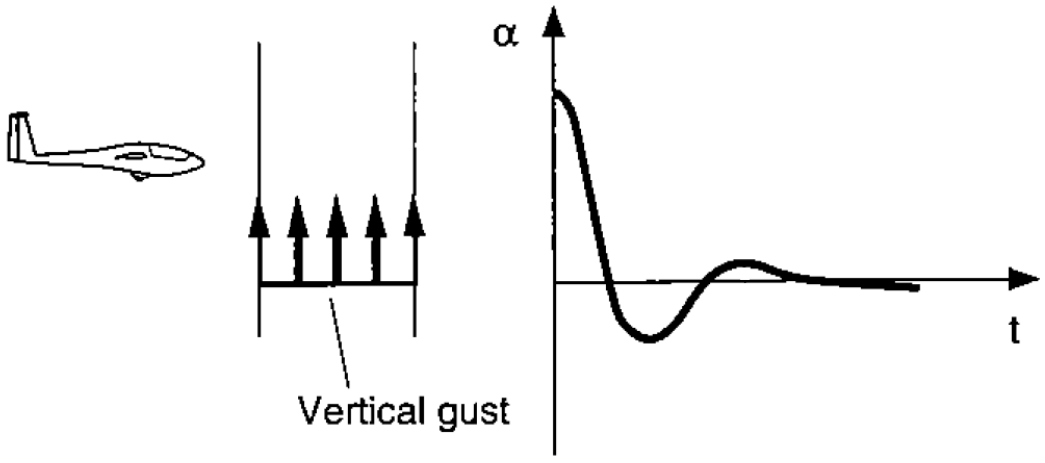

Figure 6: The short-period mode (Tomas & Milgram 1999)

Figure 6 shows the short-period mode. This mode can be excited by flying through a sharp-edged vertical gust for example. This mode is characterised by variations in pitch angle and angle-of-attack with relatively little variation in altitude and airspeed. The damping of the short-period mode depends considerably on the location of the aircrafts centre of gravity relative to the neutral point and aerodynamic damping about the pitch axis. In most sailplanes, this motion is well damped and usually dies out within a single period. Due to this the short-period mode is generally of little importance for sailplanes of conventional configuration.

2.3.2. Longitudinal static stability

In the case of sailplanes it is static stability that tends to be the more important design issue (Tomas & Milgram 1999). Static equilibrium requires that the aerodynamic forces balance the components of weight, and all aerodynamic pitching moments about the centre of gravity sum to zero.

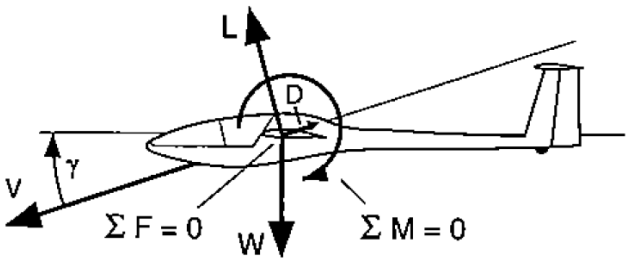

Figure 7: Equilibrium condition for un-accelerated flight (Tomas & Milgram 1999)

It is common practice in stability analysis to use the aircraft centre of gravity as the reference point for the pitching moments as it allows the moment due to weight to be ignored. Following a disturbance in equilibrium an aircraft will develop an aerodynamic pitching moment that tends to either restore equilibrium (statically stable) or lead to further departure from equilibrium (statically unstable).

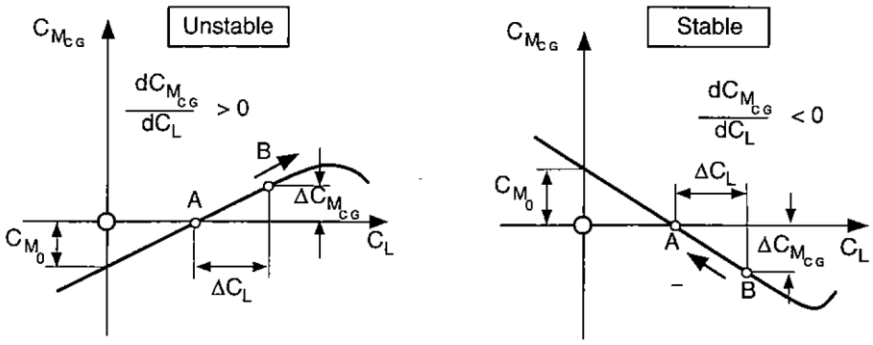

Figure 8: Unstable and stable pitching moment gradients for the complete aircraft (Tomas & Milgram 1999)

Stability is related to the pitching moment curve shown in Figure 8. A positive gradient in the pitching moment curve indicates that, following a nose-up

disturbance in equilibrium, the aerodynamic pitching moment will become more positive increasing the pitching angle and thus resulting in a statically unstable situation. A negative pitching moment gradient, on the other hand, indicates a restoring force will be generated resulting in a statically stable condition.

The equilibrium condition is observed to be at the intersection of the pitching moment curve with the x-axis. Since the lift coefficient in normal flight is always positive, a negative pitching moment gradient implies that the zero-lift pitching moment, C_{M_0}, must also be positive. Consequently longitudinal static stability is characterised by:

$$\frac{dC_{M_{CG}}}{d\alpha} < 0 \tag{2.1}$$

$$C_{M_0} > 0 \tag{2.2}$$

By themselves wings typically have a negative pitching moment due to airfoil camber and are thus fundamentally unstable. For this reason a horizontal tailplane is required to fulfil the stability criterion given by equation (2.2). The zero-lift moment of the entire aircraft may be adjusted by varying the angle of incidence of the horizontal tailplane relative to the wing. Each zero-lift moment corresponds to a certain equilibrium value of the lift coefficient of the aircraft which in turn corresponds to a particular airspeed. The pilot establishes the desired trim airspeed by using the cockpit controls to vary the deflection of the elevator δ_e.

2.3.3. Pitching moment equilibrium

An aircraft is in moment equilibrium when the sum of all moments about its centre of gravity is zero.

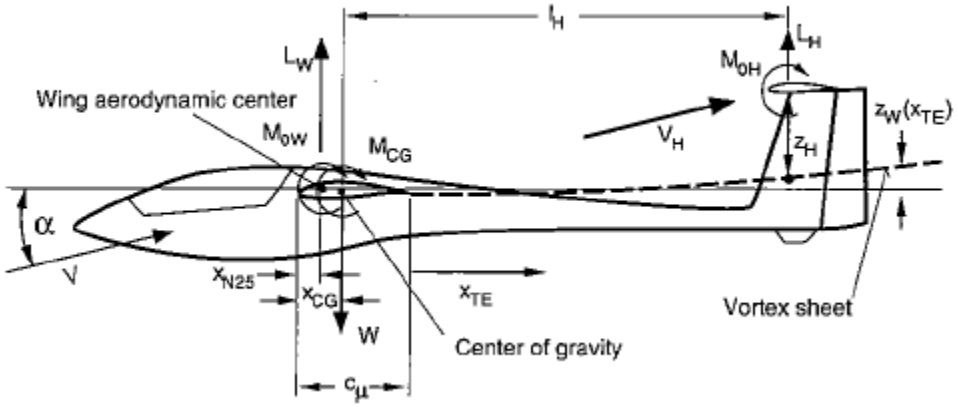

Figure 9: Force and moment definitions for longitudinal stability analysis (Tomas & Milgram 1999)

This condition is summarised in equation (2.3):

$$M_{CG} = L_W(x_{CG} - x_{AC}) + M_{0W} - l_H L_H = 0 \tag{2.3}$$

Here the longitudinal stations x_{CG} and x_{N25} are measured from the leading edge of the mean aerodynamic chord, c_μ, of the wing. An exact calculation would take into account the aerodynamic moments of both the horizontal tailplane and fuselage and the effect of elevator deflection. These factors will be ignored in this section to simplify the explanation of the important aspects.

Equation (2.3) can be written in non-dimensional form by normalising to the dynamic pressure q, wing area S_W and the mean aerodynamic chord c_μ:

$$C_{M_{CG}} = C_{L_W} \frac{x_{CG} - x_{AC}}{c_\mu} + C_{M_{0W}} - C_{L_H} \frac{l_H S_H}{c_\mu S_W} = 0 \tag{2.4}$$

C_{L_W} is the lift coefficient of the wing, approximately equal to the lift coefficient of the entire sailplane depending on the position of the centre of gravity. $C_{M_{0W}}$ is the zero lift coefficient of the wing alone, S_H is the horizontal tailplane surface area, l_H the moment arm between the centre of gravity and aerodynamic centre of the horizontal stabiliser and x_{AC} the location of the aerodynamic centre of the isolated wing. Usually, $x_{AC} \approx \frac{1}{4}c_\mu$. For longitudinal stability, the quantity of interest is the moment gradient. This is obtained by differentiating the equilibrium equation given by equation (2.4). Here it is assumed that $C_{L_W} = C_L$:

$$\frac{dC_{M_{CG}}}{dC_L} = \frac{dC_{M_{CG}}}{dC_{L_W}} = \frac{x_{CG}}{c_\mu} - \frac{1}{4} - \frac{dC_{L_H}}{d\alpha_H}\frac{d\alpha_H}{d\alpha}\frac{d\alpha}{dC_{L_W}}\frac{l_H S_H}{c_\mu S_W} \tag{2.5}$$

For convenience the horizontal tail volume is introduced:

$$V_H = \frac{dC_{L_H}}{d\alpha_H} l_H S_H \tag{2.6}$$

The horizontal tailplane operates in the induced velocity field of the wing and its angle-of-attack is decreased by the downwash angle at the horizontal tailplane location produced by the wing denoted by α_W. Furthermore the wing and horizontal tailplane are usually set at different angles of incidence with respect to the fuselage reference axis. The angle between the fixed portion of the horizontal tailplane and fuselage reference axis is the horizontal tailplane incidence angle ε_H.

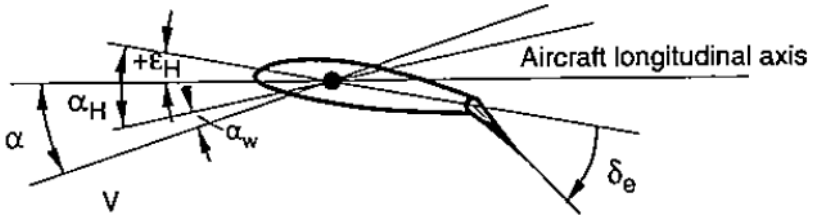

Figure 10: Horizontal tailplane angle definitions (Tomas & Milgram 1999)

Figure 10 gives the angle definitions for the horizontal tailplane. From this figure it can be seen that:

$$\alpha_H = \alpha + \varepsilon_H - \alpha_W \tag{2.7}$$

The induced downwash angle is in turn a function of wing angle of attack. Differentiating equation (2.7) with respect to α leads to:

$$\frac{d\alpha_H}{d\alpha} = 1 - \frac{d\alpha_W}{d\alpha} \tag{2.8}$$

This leads to:

$$\frac{dC_{M_{CG}}}{dC_L} = \frac{x_{CG}}{c_\mu} - \frac{1}{4} - \left(1 - \frac{d\alpha_W}{d\alpha}\right)\left(\frac{dC_{L_W}}{d\alpha}\right)^{-1} \frac{V_H}{c_\mu S_W} \tag{2.9}$$

From equation (2.9) the influence of the horizontal tailplane on the pitching moment gradient and thus longitudinal stability can be determined. Figure 11 shows this influence graphically. Curve “a” shows the pitching moment curve for the wing alone which is unstable. Curve “b” shows the stabilising contribution of the horizontal tailplane and curve “c” the pitching moment curve for the entire aircraft which is stable.

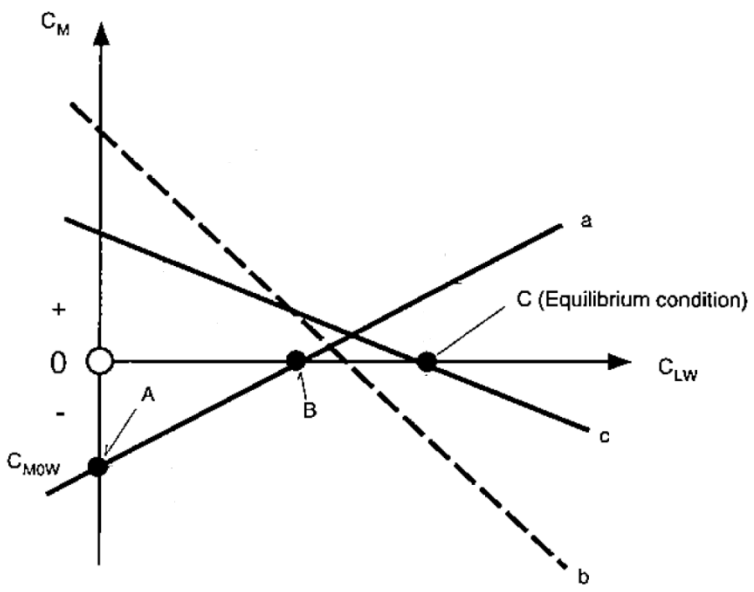

Figure 11: Horizontal tailplane contribution to longitudinal stability (Tomas & Milgram 1999)

2.3.4. Significance of the centre of gravity and neutral point location

Analogous to the aerodynamic centre of an isolated wing, a neutral point is defined for the complete aircraft. This is the point about which the sum of the aerodynamic pitching moments is independent of the aircraft's lift coefficient. This definition allows the aerodynamic loads acting on the aircraft to be expressed as a combination of lift and a constant pitching moment where the lift of the aircraft varies with angle-of-attack and the constant pitching moment is controlled by the pilot via elevator inputs.

The location of the sailplane centre of gravity relative to its neutral point provides a convenient measure of equilibrium and static stability. With the centre of gravity ahead of the neutral point the lift acting on the neutral point contributes to a nose-down pitching moment. A slight increase in angle-of-attack leads to an increase in both wing and horizontal tailplane lifts. The lift of the wing and horizontal tailplane act in combination at the aircraft's neutral point by definition thus producing a nose-down pitching moment about the centre of gravity. This stable behaviour stands in contrast to the case where the centre of gravity lies behind the neutral

point. In this situation the additional lift creates a nose-up pitching moment rendering the aircraft statically unstable.

Longitudinal static stability is thus present if and only if the centre of gravity lies ahead of the neutral point:

$$x_N - x_{CG} > 0 \tag{2.10}$$

Moment equilibrium at the centre of gravity requires:

$$C_{M_{CG}} = -C_L \frac{x_N - x_{CG}}{c_\mu} + C_{M_0} \tag{2.11}$$

Differentiating equation (2.11) with respects to C_L yields:

$$\frac{dC_{M_{CG}}}{dC_L} = \frac{x_{CG}}{c_\mu} - \frac{x_N}{c_\mu} \tag{2.12}$$

By equating the left hand side of equations (2.9) and (2.12) the neutral point can be determined as a percentage of the mean aerodynamic chord of the wing.

Equation (2.12) provides a criterion for ensuring longitudinal static stability. Since the restoring moment following an angle of attack change is proportional to the left hand side of this equation, it provides a measure of stability referred to as the static margin. The greater the static margin the greater the tendency of the aircraft to return to its equilibrium condition following a disturbance in pitch.

For a given aircraft, the magnitude and direction of the horizontal tailplane lift is largely a function of the centre of gravity location. At aft centre of gravity locations, where the stability margin is low, very little horizontal tailplane lift is required to change the equilibrium lift coefficient of the aircraft. As the static margin is increased, higher lift forces are required resulting in an increase in the drag contribution from the horizontal tailplane called trim drag. For this reason an excessive static margin is undesirable in sailplanes. Sailplanes are typically designed

with their aft centre of gravity limits very close to the neutral point, often within only 5 to 10% of mean aerodynamic chord (Tomas & Milgram 1999).

2.3.5. Sailplane flight envelope

General flight envelope requirements are given in subpart C of the CS-22. Sailplane flight envelope is given by the combination of the manoeuvring and gust envelopes. By definition manoeuvers involve transient conditions which arise from changing from one trim condition to another (Tomas & Milgram 1999). Not only must the structure of a sailplane be designed for loads given by the gust and manoeuvring envelopes, elevator authority must also be sufficient to perform these manoeuvers. The manoeuvring envelope for sailplanes given by the CS-22 is shown in Figure 12:

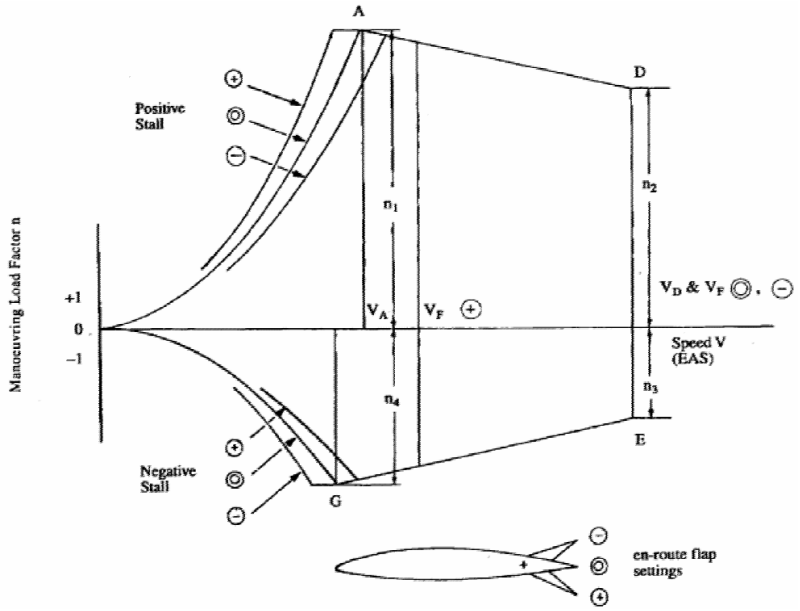

Figure 12: Manoeuvring envelope

The manoeuvring envelope is defined by four fixed load factors. The load factors for a utility sailplane are given in Table 1. The design manoeuvring speed is given by equation (2.13).

$$V_A = V_{s1}\sqrt{n_1} \tag{2.13}$$

Where V_{s1} is the stall speed of the wing with flaps in neutral position and airbrakes retracted.

Category	U
n_1	+5·3
n_2	+4·0
n_3	−1·5
n_4	−2·65

Table 1: Manoeuvring envelope fixed load factors

V_D is the design maximum speed of the sailplane and V_F is the flap design speed. The load factors for airspeeds below V_A are given by equation (2.14).

$$n = \frac{\rho_0 V^2 C_{Lmax} S_w}{2Mg} \tag{2.14}$$

This process can be repeated to give the manoeuvring envelope for each flap setting thus giving the load factors at which the horizontal tailplane will be required to give maximum lift expected. The gust envelope for sailplanes given by the CS-22 is shown in Figure 13.

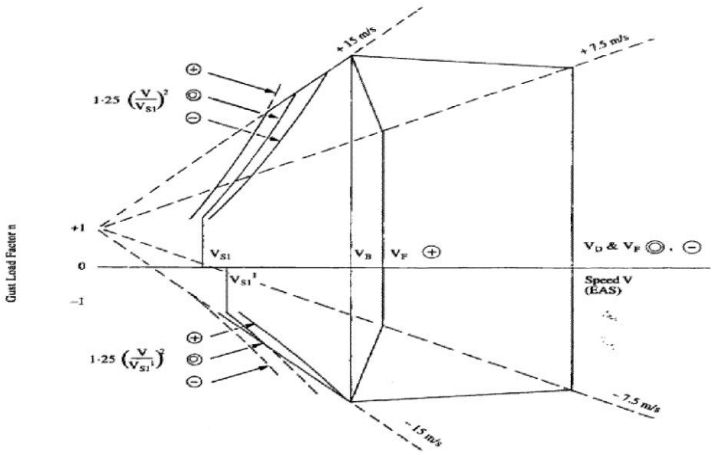

Figure 13: Gust envelope

For the gust envelope, load factors for airspeeds below V_B are given by the lesser of the following:

$$n = 1.25\left(\frac{V}{V_{S1}}\right)^2 \tag{2.15}$$

$$n = 1 \pm U\left(\frac{dC_{LW}}{d\alpha}\right)\frac{k\rho_0 VS}{2Mg} \tag{2.16}$$

For airspeeds above V_B the load factor is given by line connecting the value of equation (2.16) with $U = 15\,m/s$ and $V = V_B$ and the value of equation (2.16) with $U = 7.5\,m/s$ and $V = V_F$ *or* V_D.

From these envelopes the maximum expected elevator deflection for each wing flap setting over their permitted airspeed range can be calculated. A constraint can be applied to this value to ensure that the horizontal tailplane will operate in the airfoil's permitted elevator deflection range.

2.3.6. Influence of the horizontal tailplane on total sailplane drag

The lift created by the horizontal tailplane needed for aircraft stability results in an increase of drag. This is due to the added area and drag due to lift. This drag contribution is called trim drag. In a lecture given by Boermans (2006) the influence of the ASW-27's wing, tailplanes and fuselage on its speed polar was given (see Figure 14).

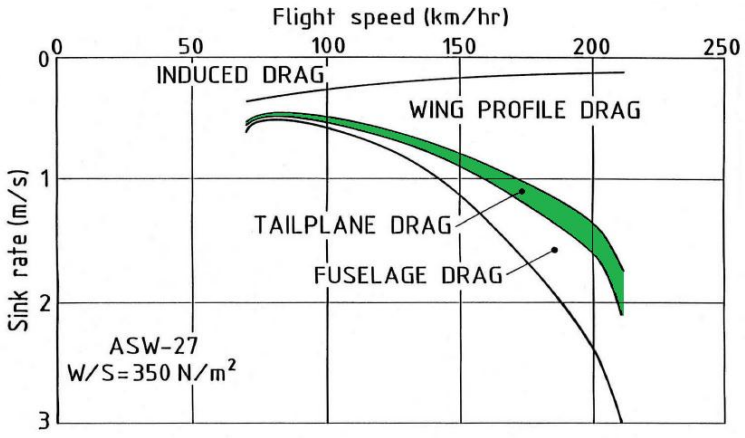

Figure 14: Contribution of aerodynamic components to the ASW-27's speed polar

The tailplane increment marked in green in Figure 14 shows the influence of the vertical and horizontal tailplanes. The percentage of total drag created by the horizontal tailplane was calculated by assuming the drag created by the horizontal tailplane is proportional to the planform area of the horizontal tailplane and that interference drag is negligible. Figure 15 shows the percentage of total drag of the combined horizontal and vertical tailplanes and the horizontal tailplane alone for airspeeds of 100 to 200 km/h. It is seen that the percentage of total drag for the horizontal tailplane varies between 3.5 and 4.8%. Due to this small percentage, a relatively small drag reduction in respect to total sailplane drag can be expected.

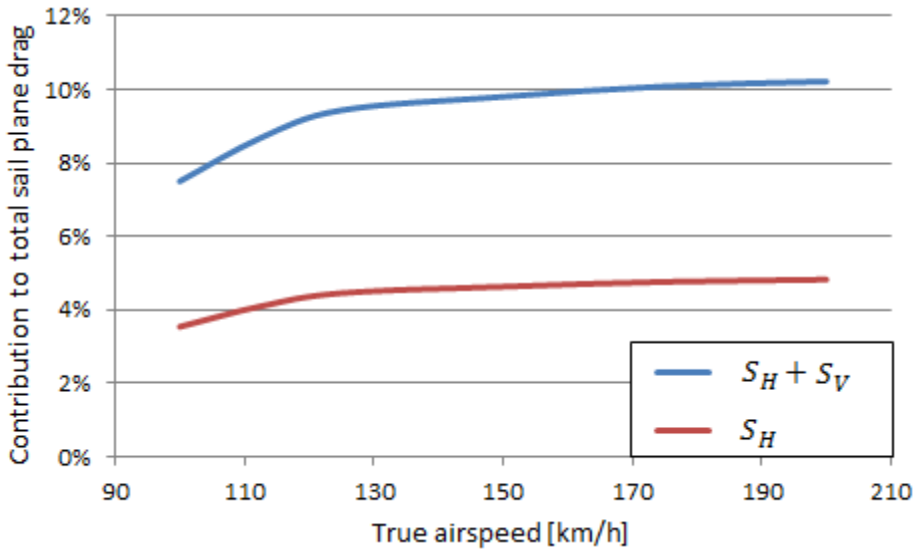

Figure 15: Drag contribution of the horizontal tailplane to the total drag of the ASW-27

2.4. Influences of wing shape on drag

Two main components of drag are present in finite wings drag due to lift and profile drag. Both these components are heavily dependent on the planform shape of a wing, their optimums, however, are contradictory. The following section will concentrate on the relationship of these drag components and influences of wing shape on the drag of wings.

2.4.1. Induced drag

Drag due to lift indicates components of drag associated with the generation of lift. Drag due to lift and its many variants is called induced drag due to the similarity of the fluid dynamic flow pattern with that of the magnetic fields induced by electric conductors (Glauert 1983). These induced vortices are an essential part of the vortex system behind the wing due to the fact that they are the means through which momentum is transferred from the flying wing to the fluid (Hoerner 1965).

The primary function of a wing, lift, is produced by deflecting a stream of fluid downward from its undisturbed direction. For infinite span, as in the case of airfoils, the affected volume of fluid is infinite as well. For a uniform lift distribution the remaining deflection angle and induced drag are zero. Due to the limited span of finite wings, however, induced drag is the penalty paid for producing the needed lift given by the wings operational requirements.

Theory indicates that the optimum lift distribution over the span of a wing, providing maximum lift for a given angle-of-attack and minimum induced drag for a given value of lift, is elliptical. A comparison of various planform shapes and wingtip geometries is given in Hoerner (1965). Three families of wing planforms were evaluated and are given in Figure 16.

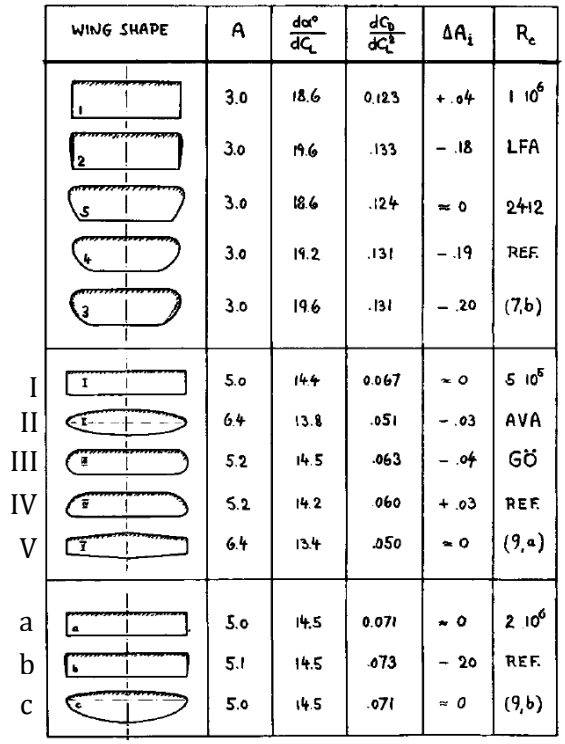

Figure 16: Families of wing planforms (Hoerner 1965)

From Figure 16 it can be seen that the most effective planforms were the rectangular, moderately tapered and those with long trailing edges. The cut-away shapes (3,4) and elliptical wings (II,c) were less effective. It was found that induced drag can be reduced by making the effective span of the wing as wide as possible as it is favourable to keep the tip vortices apart from each other as far downstream possible.

In low aspect ratio wings the lateral edges have an important influence on lift and drag. The flow around the tips can go around the lateral edge due to the wake roll-up (Figure 17). This decreases the effective span of the wing and allows the trailing vortices to have a larger effect on induced drag.

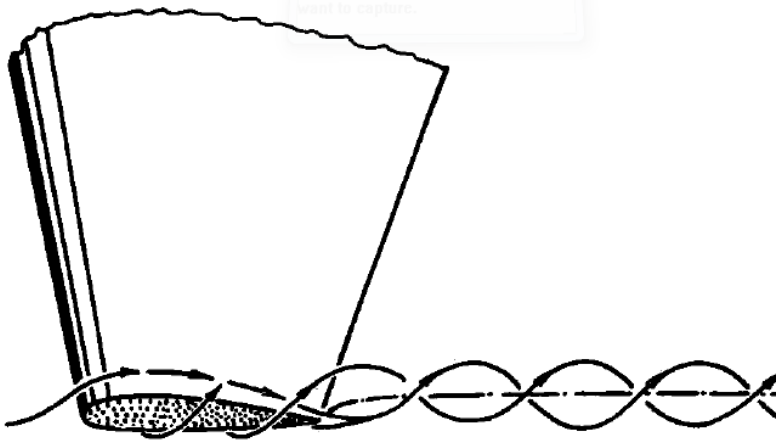

Figure 17: Flow pattern past a wing tip (Hoerner 1965)

Six wingtip shapes were also evaluated on a rectangular wing. Figure 18 shows the vortex core location. It was found that wingtips with sharp lateral edges have the widest spans while rounded tips resulted in a loss of effective span and thus aspect-ratio.

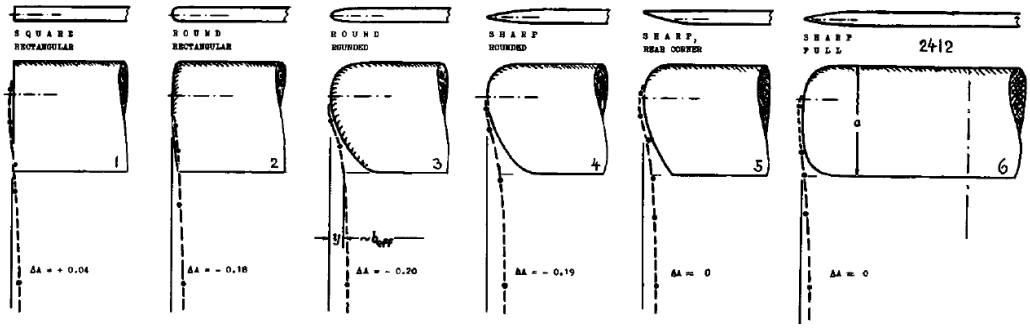

Figure 18: Wing tip shape and tip vortex location of the evaluated wingtips (Hoerner 1965)

Figure 19 shows a comparison of the lift and drag characteristics of wings 1, 2 and 5 from Figure 18. It is seen that the tip shapes with the widest vortex spans are generally the ones with the lowest induced drag. It is also seen that the square and sharp tips gave the similar drag values at the same lift coefficient values.

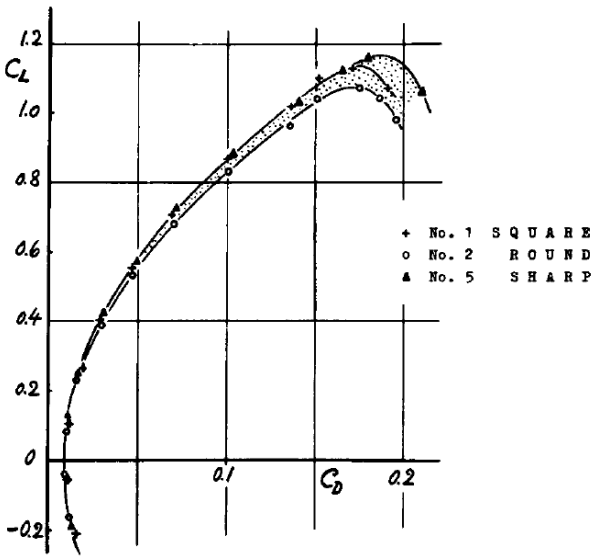

Figure 19: Lift and drag characteristics for wingtips 1, 2 and 5 (Hoerner 1965)

In conclusion, after taking into account the influence of wing planform shape and wingtip effects, a combination of a moderately tapered wing planform and wingtip 5 would be the most effective. Furthermore the shape of the wingtips can be more important than the planform of the wing in the higher lift region.

2.4.2. Profile drag

Profile drag of wings is treated as a predominantly two-dimensional drag component. For this reason the airfoil shape of the wing is important. Although this study will only concentrate on planform design it is necessary to assess the impact of the planform shape on the airfoils and thus profile drag. Two aspects dominate the development of airfoils; firstly the influence of Reynolds number and secondly the shape most suitable for its application (Hoerner 1965).

The first aspect is of particular importance as the planform shape of a wing has an influence on the local span-wise Reynolds numbers. When comparing planform shapes of the same area but different aspect ratios it is seen that the planform with the higher aspect ratio is characterised by smaller chord lengths across its span.

This reduces the local span-wise Reynolds numbers which in turn increases the profile drag of the wing. This is in direct contradiction with reduction of induced drag. Figure 20 shows the influence of Reynolds number on the profile drag on airfoils. It is seen from this figure that profile drag steadily decreases with the increase of the Reynolds number. From Reynolds numbers of 10^6 and higher, airfoil flows have the tendency to fall in three categories - laminar flow, transitional flow where laminar and turbulent flow is present and fully turbulent flow.

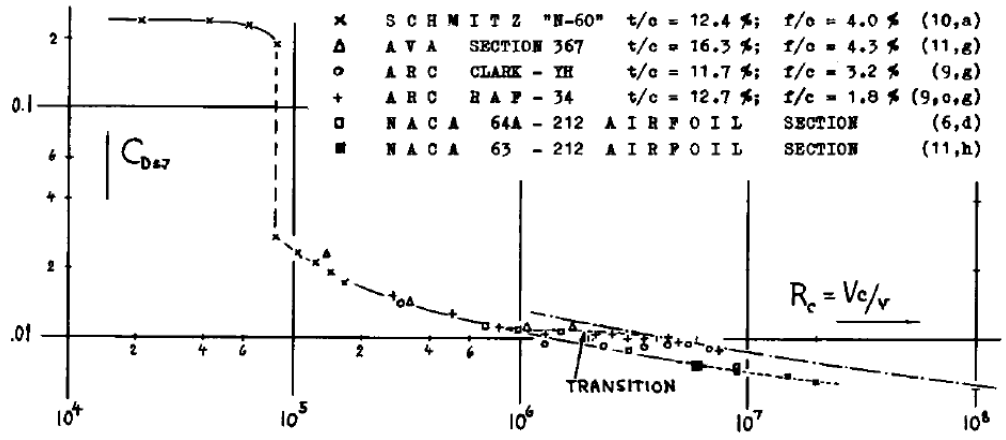

Figure 20: Influence of Reynolds number on profile drag of airfoils (Hoerner 1965)

The airfoils on horizontal tailplanes used on sailplanes usually operate at low Reynolds numbers, typically from values of 500000 to 1500000 (Boermans & Bennis 1991). At these low Reynolds numbers the flow is fundamentally different and more complicated than at high Reynolds numbers. In this region the laminar boundary layer usually separates and become unstable while separated and transitions to turbulent flow in “mid-air” after which the flow reattaches to the airfoil surface. The laminar separation, transition to turbulence, turbulent reattachment and recirculating flow captured is called the laminar separation bubble (Figure 21). This process is accompanied by large energy losses and is the principal reason for degradation of performance of airfoils at low Reynolds numbers (Selig 1989). The use of artificial transition control is used extensively on the wings of modern sailplanes and has been implemented in the design of a Standard Class

sailplane horizontal tailplane airfoil by Boermans & Bennis (1991). This technique avoids laminar separation bubbles and makes longer laminar flow regions possible.

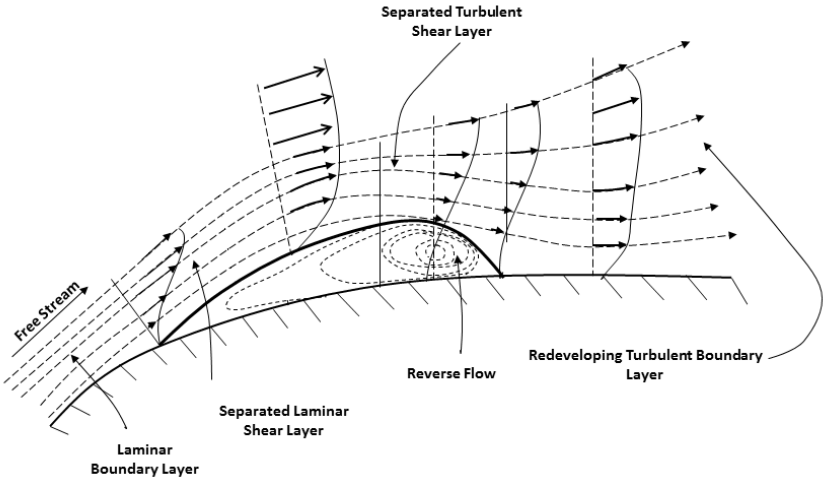

Figure 21: The laminar separation bubble

An investigation into the influence of wingtip shapes on profile drag is given in Hoerner (1965). The wingtips tested correspond to wingtips 1, 2 and 5 in Figure 18. Figure 22 shows the distribution of profile drag found in the wake of these wingtips viewed from the trailing edge compared to the two dimensional profile drag distribution. Negative values were found in two (2, 5) of the wingtips after integrating the two-dimensional and wake distributions and subtracting the values. From this it can be concluded that the profile drag of wings of finite span is less than in two dimensions.

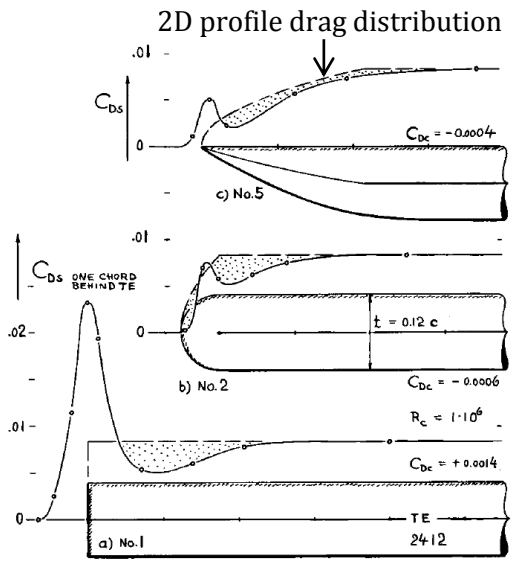

Figure 22: Distribution of profile drag within the wake of wingtips 1, 2 and 5 (Hoerner 1965)

2.5. Optimisation philosophies for horizontal tailplanes used on sailplanes

As with the wing the primary horizontal tailplane planform parameters are aspect ratio sweep and taper. Early sailplane designs generally favoured rounded horizontal tailplane planforms due to the reduced induced drag as a result of their nearly elliptical lift distribution. In modern sailplanes trapezoidal planforms are used due to their reduced complexity in regards to manufacture and have proven acceptable and even better in an aerodynamic point of view as was seen in section 2.4.

The optimum aspect ratio for the horizontal tailplane is a function of the profile drag of the selected airfoil, induced drag, weight considerations and the effects of the lift curve slope. Various studies have shown that horizontal tailplane aspect ratios in the range of 5 to 8 yield good results (Tomas & Milgram 1999).

A study by Maryland (1979) set out to assess the influence of horizontal tailplane modifications on the total drag of a standard class sailplane. In his study two parameters were varied, the planform area and the span of the horizontal tailplane.

It was found that it was suitable to design the horizontal tailplane with the minimum possible area that would still satisfy stability requirements. Furthermore the optimum aspect ratio was also investigated. It is well-known that with the increase of wing span induced drag is reduced. An increase in span has a negative effect on profile drag; however, due to the decreasing span-wise local Reynolds numbers. Due to the low horizontal tailplane lift needed to satisfy stability it was found that the reduction of induced drag due to higher horizontal tailplane span is less important than the influence of profile drag.

2.6. Aerodynamic optimisation methods

As in the case of most engineering optimisation problems, aerodynamic shape optimisation is a constrained non-linear problem. Hicks & Henne (1978) published one of the first papers on aerodynamic shape optimisation. A first order gradient-based algorithm in conjunction with an inviscid flow solver was used to optimise the shape of a wing with respect to design criteria. Since then aerodynamic shape optimisation has become an active field of research producing several innovative methods for aerodynamic shape optimisation of airfoils (Numec, Zingg & Pulliam 2004) and wings (Giraldo, Garcia & Boulanger 2008).

With a relatively expensive objective function that cannot be avoided with flight data-based optimisation, it will be impractical to employ global algorithms such as genetic algorithms or simulated annealing due to the relatively large number of iterations (and thus function evaluations) required to find a global minimum or maximum. It is thus necessary to employ local algorithms in this study.

Local algorithms can be sub-divided into methods that make use of the gradients of the objective function and gradient-free methods.

2.6.1. Gradient-free methods

Gradient-free methods do not make use of the objective function's gradient to determine where to sample in the design space. The objective function is evaluated at a set of points instead. The function values are then compared to decide where in the design space to sample next.

The best known gradient-free method, the simplex method, was proposed by Nelder and Mead (1965). For a given starting point in an n-dimensional space, a simplex with $n + 1$ vertices is formed. The edges of this simplex can be considered to be vectors that can span the entire design space. From the initial simplex the function values at the vertices can be ordered from best to worst. Next a new function evaluation is carried out at the point where the worst point reflects through the opposing edge. The simplex can either expand or contract depending on the function

values found. In the subsequent iterations expansion, contraction and retraction is the basic moves the simplex can make to move to a minimum. This algorithm has some advantages, notably robustness for small numbers of design variables. It has, however, been found that this algorithm can fail when it is applied to a noisy objective function (Sturdza 2003). Furthermore the number of objective function evaluations needed exceeds that of the gradient-based methods making this method computationally expensive.

2.6.2. Gradient-based methods

Unlike gradient-free methods, gradient-based methods make use of the objective function's gradient to determine where to sample next in the design space. The gradient can be seen as a vector pointing in the direction of steepest descent. These methods can be sub-divided into first and second-order methods. The first-order method makes use of only the first order gradient while the second-order methods use second-order derivatives as well.

Numerous gradient-based methods have been proposed and implemented. The general idea of gradient-based methods is to start from an initial guess and evaluate the objective function and its constraints and move one step size in every direction of the design space. Next the gradients of each evaluation are compared. From the gradient information the next sampling point is chosen. This process is repeated until no improvement is possible. The gradient descent associated with this method is shown in Figure 23.

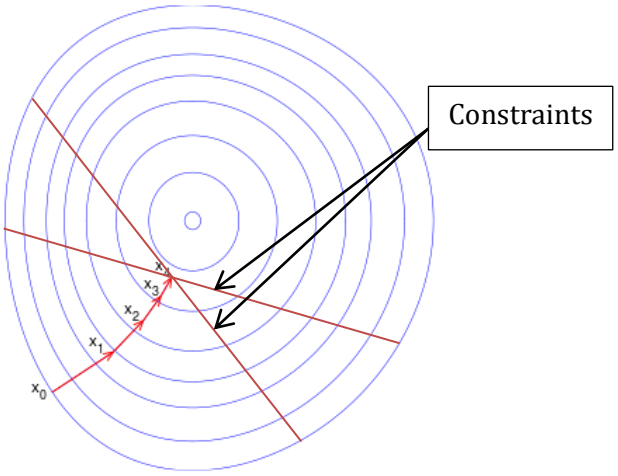

Figure 23: Gradient descent in a two dimensional space

The speed and accuracy of this method make this method desirable in multi-point optimisation. Each of the iterations in a n dimensional space needs $n+1$ evaluations of the objective function and its constraints. The design space for a horizontal tailplane of N tapered sections will consist of $2N+1$ dimensions if the root and tip chord and section area is varied. The number of wing sections that will be used is not expected to exceed 5, for this reason gradient-based methods are a prime group of candidates for this study.

2.6.3. Previous work in flight data based aerodynamic optimisation

Scherrer (2008) proposed a multi-point optimisation method for the main wing of a sailplane based on his Flight Template concept. This concept weights performance as a function of the lift coefficients calculated from flight data. The objective function was based on the power absorbed by the wings drag over flight duration. Both the wing planform and a single airfoil section were optimised for a 15m class sailplane.

For the wing planform case aerodynamic coefficients of interests were calculated by the extended lifting line theory developed by Sivells & Neely (1947). Trends showed the aerodynamic optimum for minimum power absorbed by drag tend to be around

$AR = 30$. This is reasonably high for 15m sailplanes where the common aspect ratio currently used tends to be closer to $AR = 27$.

2.7. Finite wing analysis methods

Unlike the two-dimensional flow assumed in airfoil analysis, the flow over finite wings is three-dimensional. This means that spanwise flow is also possible and unavoidable. This gives rise to the well-known tip vortices and the associated lift induced drag called induced drag.

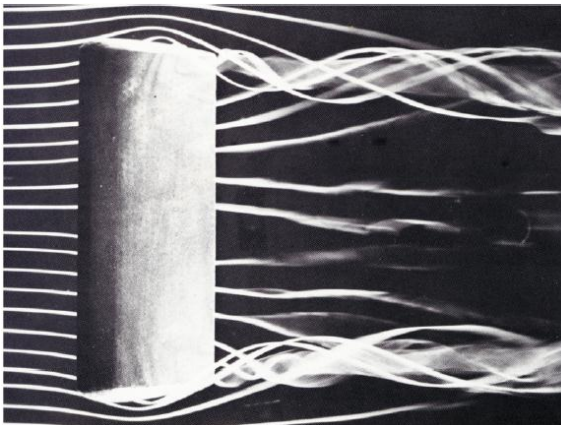

Figure 24: Flow over a finite wing (van Dyke 1983)

There are four wing analysis methods used in the design of modern sailplanes. These are, in ascending order of complexity, the lifting line theory, Vortex-Lattice method, 3D Panel methods and Navier Stokes methods.

2.7.1. The lifting line theory

The lifting line theory has been used with success in the design of the ASW-24 (Boermans & Waibel 1989). In this relatively simple inviscid method the wing is divided into N spanwise sections. A bound horseshoe vortex is placed on the lifting line of the wing. The strength of each of the trailing vortices of the horseshoe vortex is equal to the change of circulation along the lifting line. Each of the trailing vortices induces a velocity on each of the sections. This leads to a linear system of algebraic equations which can be solved for the unknown circulation associated with each

section. From the circulation distribution the lift distribution, total lift and induced drag of the wing can be calculated.

There are, however, two important limitations of the theory which should be remembered, its inaccuracy when analysing wings of low aspect ratio (<4 (Rathakrishnan 2013)) and high sweep (Sivells & Neely 1947). Due to the inviscid formulation of the lifting line theory it is unable to analyse the profile drag of wings. A modification of the method incorporating airfoil data from wind tunnel tests was developed by Sivells & Neely (1947). This method can be used to calculate aerodynamic coefficients in the nonlinear part of lift polars. Furthermore this method is able to compute profile drag coefficients by spanwise integration of the section profile drag coefficients interpolated from airfoil data at the effective angle-of-attack of each section.

This method was implemented by Deperrois (2014) in his aerodynamic analysis software XFLR 5. The necessary airfoil data is calculated by Xfoil and used in the same way used by Sivells & Neely (1947). The results were compared to NACA wind tunnel data also given by Neely et al (1947). The comparison is shown in Figure 25.

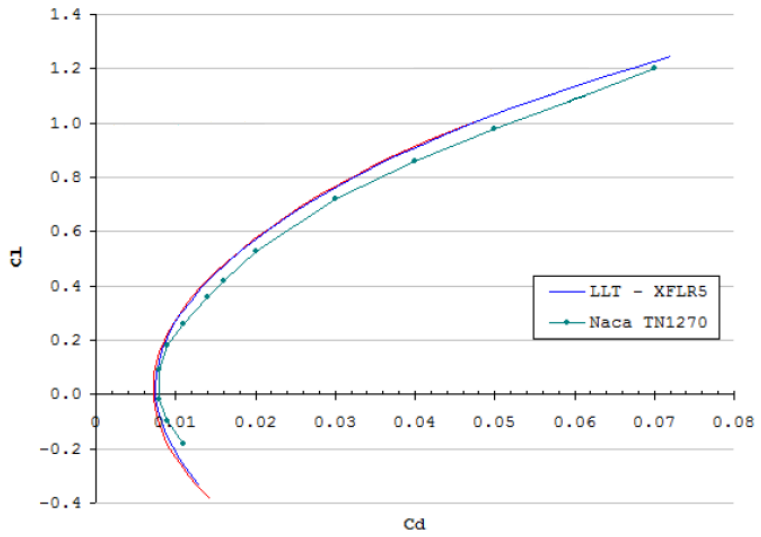

Figure 25: Comparison of the lifting line theory with wind tunnel data (Deperrois 2014)

Good comparison with experimental data can be seen for C_L values between 0 and 0.2. For higher lift coefficients under prediction of drag can be seen. Compared to

the other finite wing analysis methods, this method is computationally less expensive. This makes this method suitable when aerodynamic coefficients needs to be evaluated hundreds or even thousands of times as can be expected with flight data optimisation.

2.7.2. The Vortex-Lattice and 3D panel methods

The Vortex-Lattice method is based on solutions to Laplace's Equation. The fact that the method is strictly numerical made it unpractical until the development of computers. The method divides the wing planform into panels. A horseshoe vortex is placed on each of these panels. Along a vortex line, the circulation remains constant. The vortex line is extended to Infinity or ends at a solid boundary

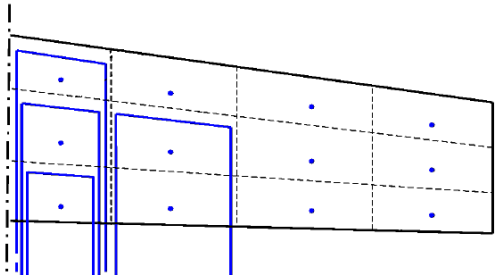

Figure 26: Discretization of the wing in the Vortex Lattice method

In the general 3D panel method the upper and lower surfaces of the wing is divided into a finite number of panels. This method can be used for both compressible and incompressible inviscid flow. A singularity is placed on each panel after which the Laplace equation is applied together with the Kutta condition on the trailing edge. This leads to a linear system of algebraic equations which can be solved. From the solution of this system the lift and drag coefficients can be calculated.

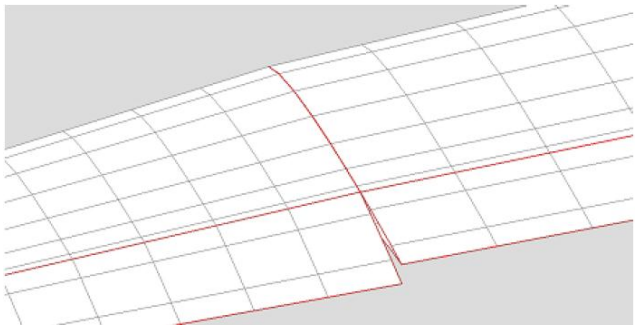

Figure 27: Wing discretization in the 3D panel method shown from the trailing edge

Deperrois (2014) implemented both these methods into his aerodynamic analysis software XFLR5. Results from both models were compared to wind tunnel test data from a F5D model sailplane. The result comparison showed under prediction of drag for both models. Both models gave good predictions of the zero angle-of-attack and lift in the linear range. In terms of computational cost the Vortex Lattice method is the less expensive of the two methods. This is due to the smaller matrix that needs to be solved. Although the better theoretical accuracy of these methods is desirable, the computational costs compared to the lifting line theory doesn't justify the accuracy gained. The lifting line theory modification given by Sivells & Neely (1947) using airfoil data will thus be used in this study.

2.7.3. Navier-Stokes methods

Hansen (2014) simulated the performance of the Standard Cirrus sailplane in steady and level flight by solving the Reynolds-Averaged Navier-Stokes (RANS) equations with the commercial computational fluid dynamics software STAR-CCM+.

The speed polar for the sailplane was calculated and compared with flight measurements performed for the Standard Cirrus. Two CFD models were constructed and solved. The first simulated the lift and drag of the wing and fuselage combination. In the second the drag of the tail section and fuselage were simulated. To account for Reynolds number effects, the drag of the tail section were simulated for all investigated velocities. The effect of transition location was also investigated

by using a fully turbulent model. Both models were discretised using an isotropic trimmed hexahedral mesh together with a prism layer consisting of 20 layers. Turbulent flow was modelled with the $k-\omega\,SST$ turbulence model and transition locations were predicted with the $\gamma - Re_\theta$ transition model.

The simulations performed using the $\gamma - Re_\theta$ transition model were seen to compare well with real flight data. Simulations matched in-flight measurements closely for velocities below 100km/h as can be seen in Figure 28. At higher velocities the sink rate were slightly under-predicted which can be expected as trim drag was neglected in the study. This method is the most computationally expensive compared to the other methods discussed. Simulation run time with this method is measured in hours which makes the use of this method impractical for use in the planform optimisation part of this study. Its accuracy, however, makes the method valuable in verification of optimisation results and the design of the tip geometry.

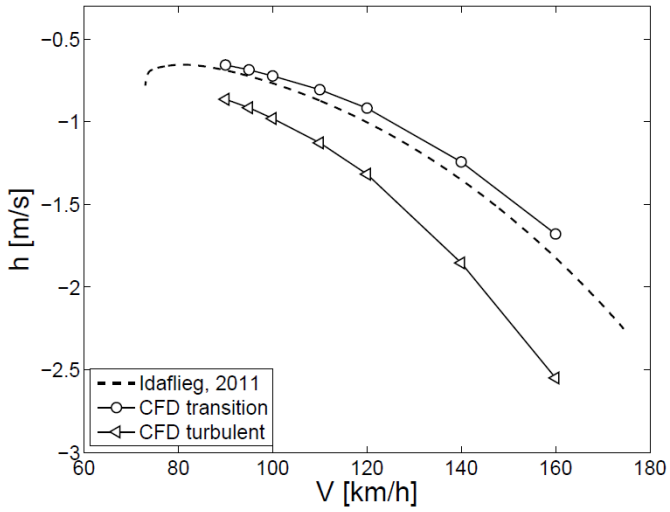

Figure 28: Standard Cirrus speed polar comparison (Hansen 2014)

2.8. Airfoil analysis methods

The finite wing analysis method to be used in this study requires airfoil data. For this reason airfoil analysis methods should be investigated. Two kinds of airfoil

analysis codes are mainly used in analysis of sailplane airfoils, panel methods and Navier-Stokes solvers.

2.8.1. Panel methods for airfoil analysis

Panel methods used in airfoil analysis are numerical methods based on simplifying assumptions about the physics and properties of the flow of air over an airfoil (Fearn 2008). The viscosity of air in the flow field is neglected while the net effect of viscosity is summarised by requiring that the flow leaves the sharp trailing edge of the airfoil smoothly.

The basic solution for panel methods consists of dividing the surface of the airfoil into flat infinitely spanned surfaces or panels. Each of these panels induces a velocity on itself and the other panels. This is modelled by distributing singularities over the panels with unknown singularity-strength parameters. Since each singularity is a solution to Laplace's equation, a linear combination of the singular solutions is also a solution. The tangent flow boundary condition is required to be satisfied at a discrete number of points called collocation points. This process then leads to a system of linear algebraic equations to be solved for the unknown singularity-strength parameters. Two codes are suited for sailplane airfoil analysis, PROFIL and Xfoil.

PROFIL (Eppler 2007) or commonly known as the Eppler code consists of a 3rd order panel method coupled with a fast integral boundary-layer calculation for analysis. The boundary layer method predicts transition using a full e^N method. Tabulated solutions to the Orr-Sommerfeld equation are used to interpolate the amplification rates of the Tollmein-Schlichting waves. These rates depend on the displacement thickness Reynolds number, the displacement to momentum-thickness shape factor and a non-dimensional frequency which is determined as the boundary layer development is calculated. The amplification of each of these frequencies is evaluated along the airfoil surface. Next the maximum frequency is found and transition is assumed when the natural logarithm of the amplification rate for any of the frequencies reaches a critical value, N. This method gives good results for attached flow for higher Reynolds numbers. At low Reynolds numbers

results tend to be less accurate due to the occurrence of laminar separation bubbles. This is the result of the inability of the integral boundary layer method to handle separation effectively. In comparison to similar codes PROFIL is very fast and robust.

Xfoil (Drela & Youngren 2001) consists of a 2nd order panel method coupled with an integral boundary layer. Iteration between the outer and inner flow solutions is continued until a stable convergence on the boundary layer displacement thickness is achieved. This allows the code to predict reasonably accurate viscous pressure distributions which capture the influence of limited trailing edge separation and laminar separation bubbles. To calculate transition Xfoil makes use of an approximate e^N-envelope method. In this method rather than tracking the amplification rates corresponding to all frequencies, only the most amplified frequency at a given point on the airfoil downstream from the point of instability is used to obtain the amplitude of disturbance. Transition is assumed when this amplitude reaches an empirically determined value. Linear approximations to actual envelopes determined using Falkner-Skan boundary layer profiles are used as amplitude curves. In comparison to PROFIL Xfoil is only slightly less robust as it has been found that convergence can occasionally be problematic.

Maugner and Coder (2010) compared predictions from Profil and Xfoil to experimental results. Profil was found to give the best prediction for the maximum lift coefficient due to the empirical correlation implemented in the code. Xfoil was found to often over-predict the value of the maximum lift coefficient. Both Xfoil and Profil produced reasonably good predictions of drag. Figure 29 shows a comparison of the drag polars calculated by Xfoil and Profil compared to experimental data. From this figure it can be seen that Xfoil gave the best overall prediction of lift and drag coefficients.

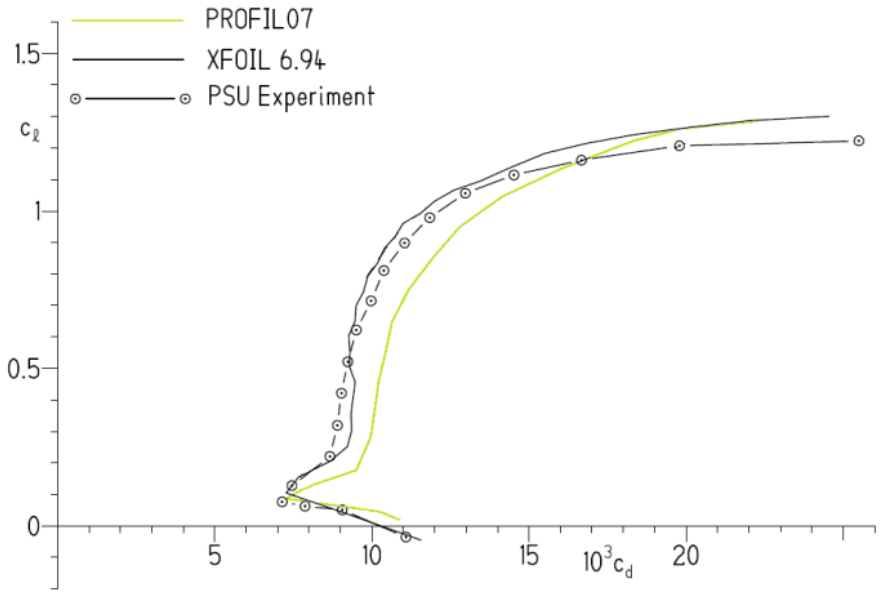

Figure 29: Comparison of Xfoil and Profil (Maugner & Coder 2010)

2.8.2. Navier-Stokes solvers

A relatively new method involves solving the Navier-Stokes equations to obtain the dimensionless coefficients of interest. Here the Navier-Stokes equations are discretised in their partial deferential form and solved over a flow field in an algebraic fashion. Due to the high computational demands of this method it only came to being as a feasible analysis and design method with the development of computers.

In the Standard Cirrus performance investigation by Hansen (2014) two dimensional simulations were conducted on the Wortmann FX 66-17 A II-182 airfoil of the Standard Cirrus outer wing panel. A structured O-mesh with y^+ values below 1 was used in conjunction with the $k-\omega$ SST turbulence model and $\gamma - Re_\theta$ transition model. The results of these simulations were compared to experimental data and results from Xfoil and Rfoil as is seen in Figure 30. It was found that the simulation results performed equally well compared to the panel methods in predicting drag coefficients at lift coefficient values between 0 and 0.6. For higher

lift coefficient values the simulation results compared better to the experiment than those of the panel methods.

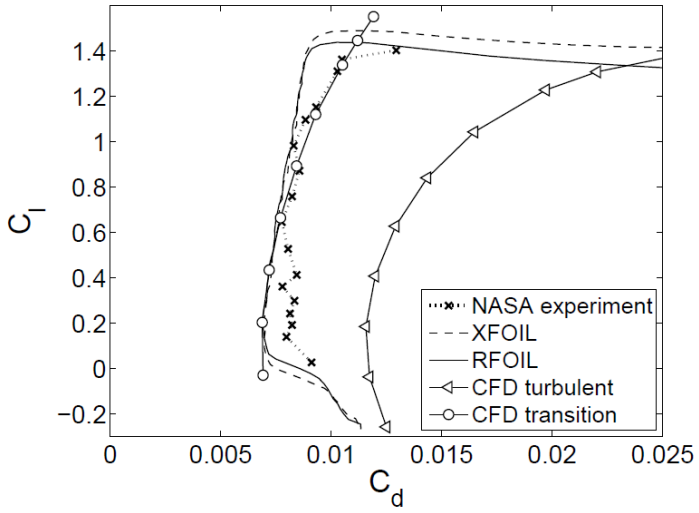

Figure 30: Comparison of CFD, Rfoil and Xfoil drag polars (Hansen 2014)

It should, however, be mentioned that grids with values of $y^+ < 1$ are relatively fine and require a lot of preparation time for the grid layout of each calculation. Furthermore, compared to panel methods where angle-of-attack sweeps can be done in a matter of seconds, Navier-Stokes solvers usually take a few minutes to calculate the aerodynamic coefficients for only one angle-of-attack.

2.9. Summary

In this chapter, applicable literature was discussed. Firstly sailplane flight was discussed giving an overview of the flight profile of sailplanes. Next the horizontal tailplane, its purpose and its influence on longitudinal stability were discussed. The influence of planform and tip section shape was also given along with design philosophies for horizontal tailplanes. Optimisation algorithms and previous work in flight data aided aerodynamic design were given next. Lastly, aerodynamic analysis methods for finite wings and airfoils were discussed and compared.

3. FLIGHT ANALYSIS

Raw IGC files contain thousands of flight points which in turn contain a number of records chosen by the pilot. The objective of the flight analysis procedure is to manipulate the raw data into a usable form. This procedure consisted of the calculation of the angle of attack and elevator deflection at each flight point. These two angles together with the airspeed and pressure altitude are required by the aerodynamic model to calculate the drag created by the horizontal tailplane at each flight point. The drag created at each flight point can then be used in the formulation of an objective function in the planform optimisation procedure. This was achieved by firstly calculating the total sailplane lift, from which the lift created by the wing and horizontal tailplane can be calculated. With the lift of the wing and horizontal tailplane known, the angle of attack and elevator deflection of the horizontal tailplane was calculated.

3.1. IGC file data processing

IGC-format files consist of lines of characters each line giving a set of data. Each line starts with an uppercase letter denoting the Record type of that line. Some of these records occur only once while others such as fixes (or B record) recur as time progresses.

Of these records the B record data contains measured data at fixed time intervals chosen by the pilot. This record contains the time of the measurement, latitude, longitude, pressure altitude, GPS altitude, true airspeed and a flight direction indicator. Of these measurements three are needed to calculate the angle of attack and elevator deflection of the horizontal tailplane at each flight point. The three important measurements and their measurement increments are given in Table 2.

Measurement	Symbol	Increment
Pressure altitude	h_p	1 m
True airspeed	V_{TAS}	1 km/h
Flight direction indicator	Ψ	1°

Table 2: Measurement increments

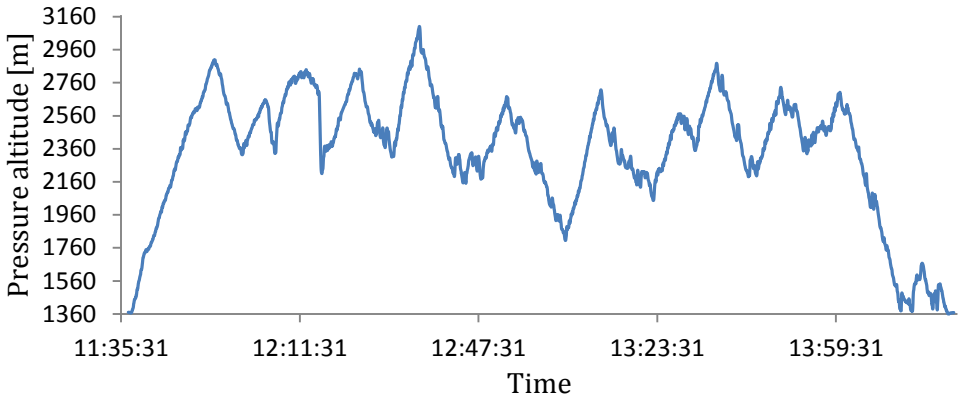

Figure 31: Pressure altitude time history of a sample flight

Figure 31 gives the pressure altitude time history of a sample flight. From the pressure altitude record the corresponding density and kinematic viscosity was interpolated from a standard sea level altitude table for each data point.

3.2. Sailplane lift

The total sailplane lift can be divided into two components. The component needed to maintain a turn and the component needed to maintain altitude or climb. Figure 32 shows the force components that act on a sailplane in a banked turn.

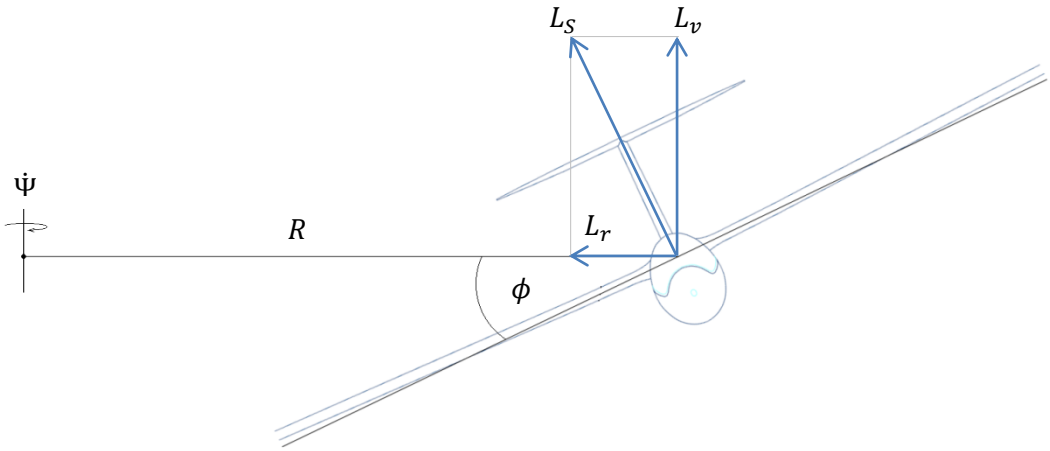

Figure 32: Total sailplane lift components

The radial or turn lift component L_r is given by:

$$L_r = ma_r \tag{3.1}$$

$$where\ a_r = \frac{{V_{TAS}}^2}{R}\ and\ R = \frac{V_{TAS}}{\Psi} \tag{3.2}$$

$$\therefore\ L_r = mV_{TAS}\Psi \tag{3.3}$$

The vertical lift component is given by:

$$L_v = m(a_v + g) \tag{3.4}$$

$$where\ a_v = \frac{d^2h_p}{dt^2} \tag{3.5}$$

Where $\frac{d^2h_p}{dt^2}$ was approximated with the second order, 7-point numerical differentiation formula from the pressure altitude time history. From these two lift components the total sailplane lift was calculated as follows:

$$L_S = m\sqrt{\left(V_{TAS}\Psi\right)^2 + (a_v + g)^2} \tag{3.6}$$

This procedure is repeated for each flight point inside the start and end times of the flight triangle.

3.3. Flight filtering

As in the case of any study implementing experimental or measured data a suitable method or criteria for elimination of outliers or doubtful data points is needed. Total sailplane lift coefficients were calculated for each flight point with the main wing area as reference area and the density interpolated from the altitude table. The true airspeed measurements are taken in 1 km/h increments by the flight logger. This

gives a total sailplane lift coefficient sub-dataset for each measured airspeed as seen in Figure 33.

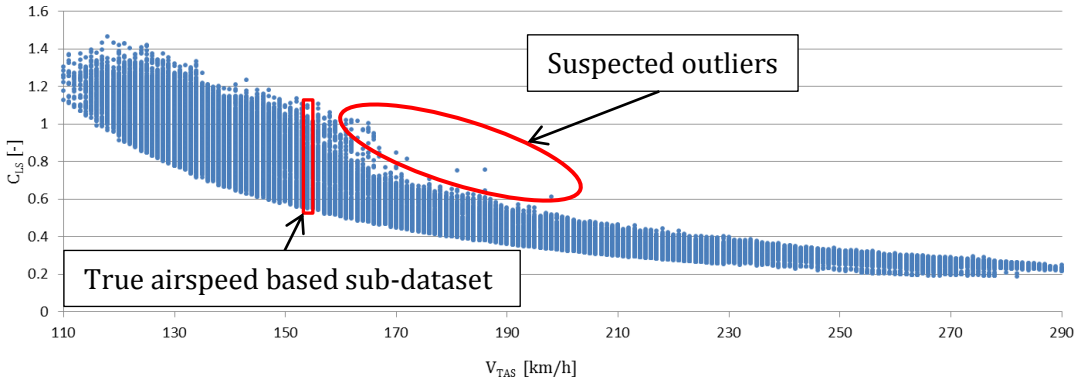

Figure 33: Total sailplane lift coefficients over the flight speed range of a sample flight

Suspicious data points in each of these sub-datasets were removed by a criterion developed by Pierce (1852). Peirce's criterion is a rigorous method based on probability theory and can be used where multiple suspicious data points are present (Ross 2003).

Data points are rejected by comparing each data point's deviation to a maximum deviation. Points are rejected when:

$$|x_i - x_m| > |x_i - x_m|_{max} \tag{3.7}$$

$$where\ |x_i - x_m|_{max} = R\sigma \tag{3.8}$$

Where σ is the standard deviation of the dataset, and R is a ratio read from a table based on the number of data points in the dataset and the number of suspected outliers. Figure 34 gives the filtered total sailplane lift coefficients.

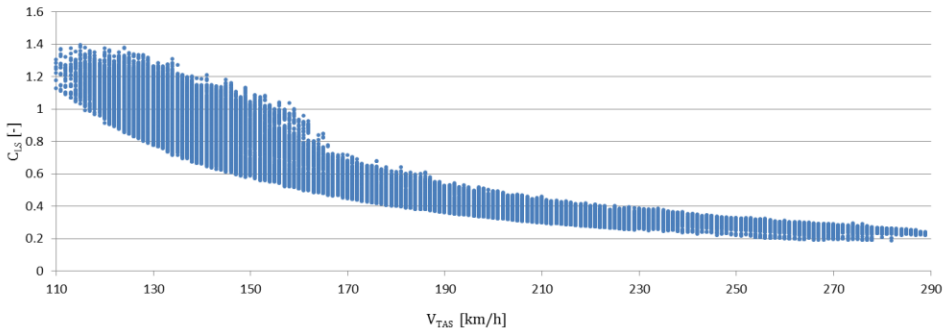

Figure 34: Filtered total sailplane lift coefficients over the flight speed range of a sample flight

Each corresponding data point to the total sailplane lift coefficient values that were rejected were removed from the flight data.

3.4. Wing and horizontal tailplane lift

The total lift of the sailplane stays fixed for each flight point irrespective of the position of its centre of gravity. Wing and horizontal tailplane lift, however, changes with centre of gravity and flap setting changes. Figure 35 shows the lift forces and moments that act on a sailplane in flight.

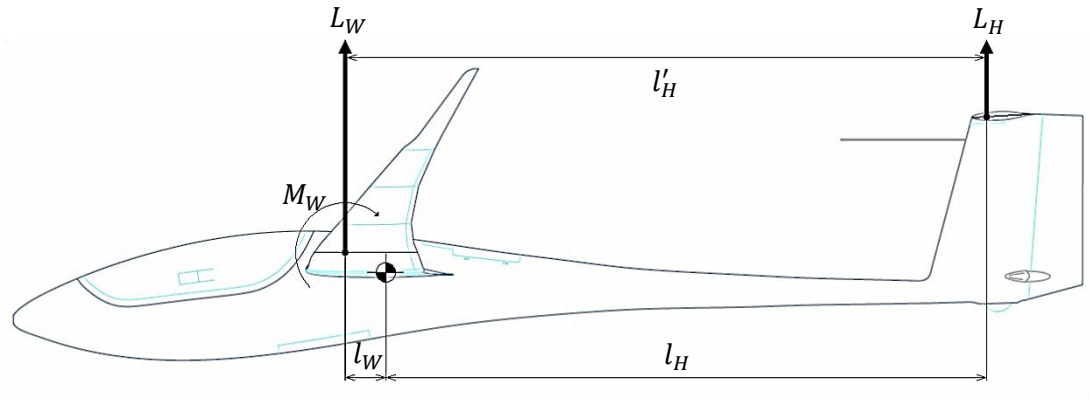

Figure 35: Wing and horizontal tailplane force diagram

The equation for the lift of the wing was derived from the forces and moments acting on the centre of gravity assuming static moment equilibrium. The effects of

horizontal tailplane drag and fuselage aerodynamic moments were neglected as the horizontal tailplane drag is small and the fuselage is designed to produce no lift. The lift of the wing is given by:

$$L_W = \frac{L_S l_H - M_W}{l'_H} \tag{3.9}$$

$$where\ M_W = qS_W \bar{c}\, C_{M_W} \tag{3.10}$$

The value of l'_H stays fixed for all centre of gravity positions as it describes the distance between the aerodynamic centres of the wing and horizontal tailplane. From l'_H and the centre of gravity position, given as a percentage of the wings mean aerodynamic chord ($\frac{X_{CG}}{\bar{c}}$), l_H can be calculated by:

$$l_H = l'_H - \bar{c}\left(\frac{X_{CG}}{\bar{c}} - 0.25\right) \tag{3.11}$$

The value of the wings moment coefficient changes with flap setting. The values for C_{M_W} for the different flap settings and respective airspeed ranges of the JS1-C 21m wing are given in Table 3.

Flap setting [°]	C_{M_W} [-]	Airspeed range [km/h]
-3	0.008	> 250
0	-0.022	190 - 250
5	-0.08	144 - 190
13.5	-0.166	100 - 144
20	-0.233	Landing

Table 3: 21m wing moment coefficients

The total lift of the sailplane is given by the sum of the lift of the wing and horizontal tailplane. From this it follows that:

$$L_H = L_S - L_W \tag{3.12}$$

The lift coefficients of the wing and horizontal tailplane are given by:

$$C_{L_W} = \frac{L_W}{qS_W} \tag{3.13}$$

$$C_{L_H} = \frac{L_H}{qS_H} \tag{3.14}$$

A sample flight was analysed for the wing and horizontal tailplane lift coefficients. The centre of gravity position was set at 45.5% of the wing's aerodynamic chord. Figure 36 shows the wing lift coefficients calculated for the sample flight. A relatively large lift coefficient range is seen for the lower flight speeds corresponding to thermal flight. This range gradually decreases with increasing airspeed.

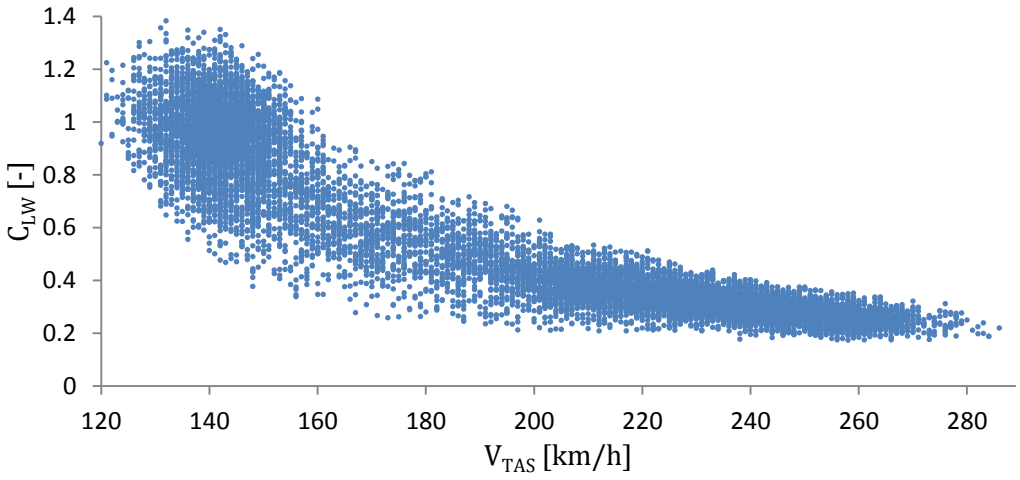

Figure 36: Wing lift coefficients over the flight speed range of a sample flight

Figure 37 shows the horizontal tailplane lift coefficients calculated for the same flight. The influence of the wing's moment coefficient change with flap settings and can be seen clearly with an upward shift. The overall range of horizontal lift coefficients varies between 0.3 and -0.15 for this flight and configuration showing

the relatively low lift coefficients the horizontal tailplane operates at confirming the importance of profile drag reduction.

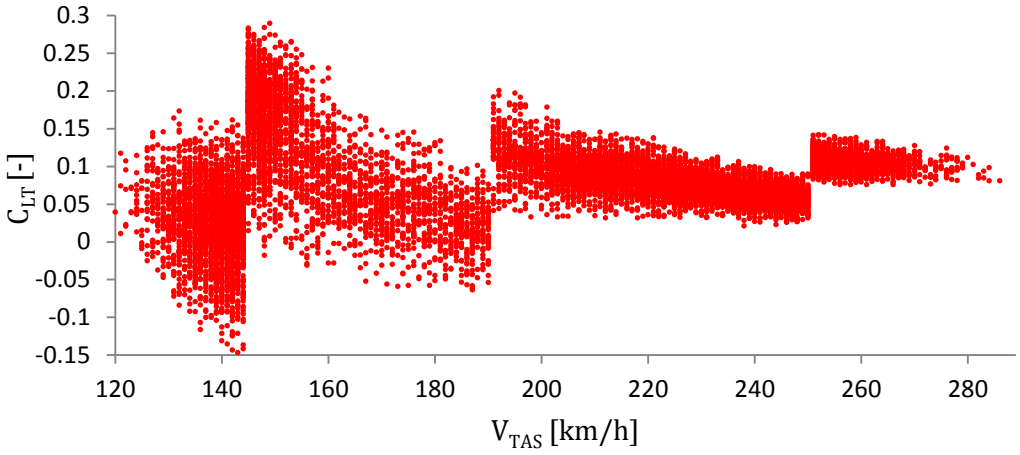

Figure 37: Horizontal tailplane lift coefficients over the flight speed range of a sample flight

3.5. Horizontal tailplane angles

The angle of attack of conventional horizontal tailplanes is heavily dependent on the angle of attack of the wing and the downward flow field or downwash produced by it. Figure 38 shows the important flow and geometric angles needed to calculate the angle of attack of the horizontal tailplane.

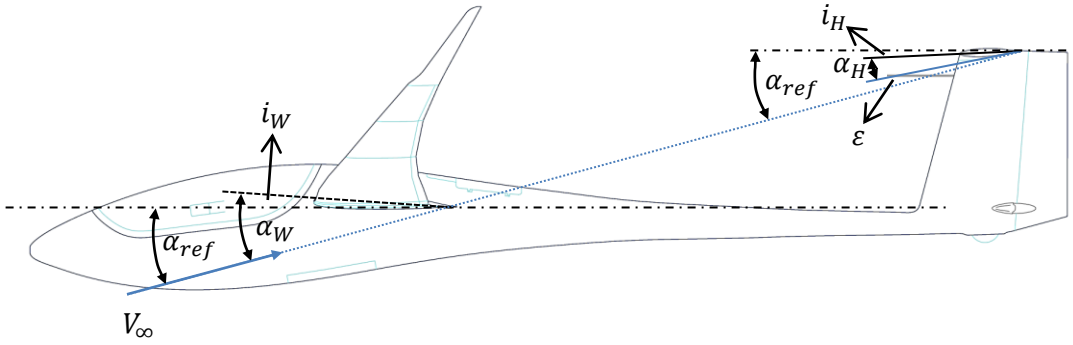

Figure 38: Horizontal tailplane flow and geometric angle definition

The wing's angle of attack, α_W, for each flight point was calculated from the wing lift coefficient of that point. The wing was assumed to operate in the linear lift region for the whole flight. The wing's angle of attack is given by:

$$\alpha_W = \frac{C_{L_w}}{C_{L_\alpha}} + \alpha_0 \tag{3.15}$$

Where C_{L_α} is the lift curve slope and α_0 the zero lift angle of attack of the wing. Both these values change with a change in flap setting and are given in Table 4 for each flap setting.

Flap setting [°]	C_{L_α} [1/rad]	α_0 [°]
-3	6.179	-0.433
0	6.404	-1.760
5	6.368	-3.968
13.5	6.178	-7.690
20	5.084	-11.250

Table 4: Lift curve slope and zero lift angle of attack for each flap setting of the JS1C 21m wing

From Figure 38 it can be shown that:

$$\alpha_H = i_H - i_W + \alpha_W(1 - \frac{\partial \varepsilon}{\partial \alpha}) \tag{3.16}$$

Where i_H and i_W is the incidence angles of the horizontal tailplane and wing and $\frac{\partial \varepsilon}{\partial \alpha}$ is the downwash curve slope. The value for $\frac{\partial \varepsilon}{\partial \alpha}$ was calculated with a method given by Silverstein and Katzoff (1939).

The elevator deflection, η_e, is given by:

$$\eta_e = \frac{1}{C_{L_\eta}}(C_{L_H} - C_{L_\alpha}(\alpha_H - \alpha_0)) \tag{3.17}$$

Where C_{L_α} and C_{L_η} were calculated with the lifting line method described in section 4.2. Figure 39 shows the calculated horizontal tailplane angles of attack for a sample flight. Large negative values are seen in the thermal flight range which can be expected due to the portion of low wing lift coefficients and subsequent low wing angles of attack that is present in this flight range. The majority of horizontal tailplane angles of attack are also negative due to the negative incidence angle of the horizontal tailplane.

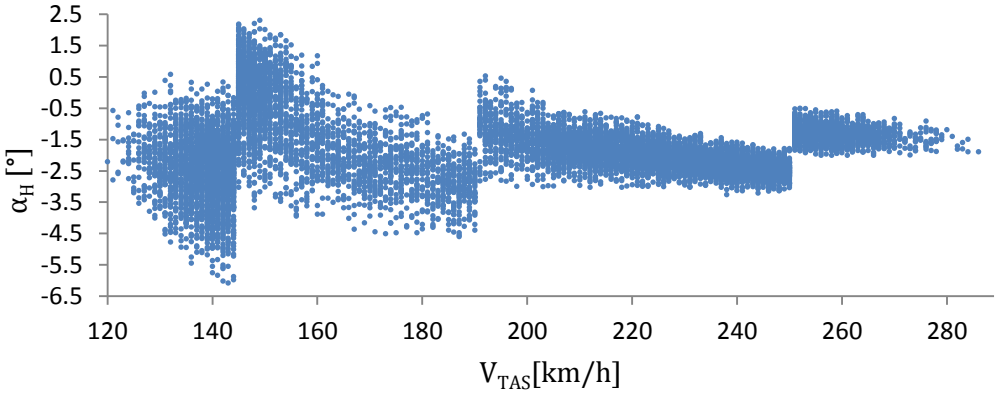

Figure 39: Horizontal tailplane angles of attack over the airspeed range of a sample flight

Figure 40 shows the calculated elevator deflections for the sample flight. The largest deflections can be seen in the higher airspeeds of the thermal flight range due to the portion of low horizontal angles of attack present. It also shows that the elevator operates in a small range in normal flight conditions.

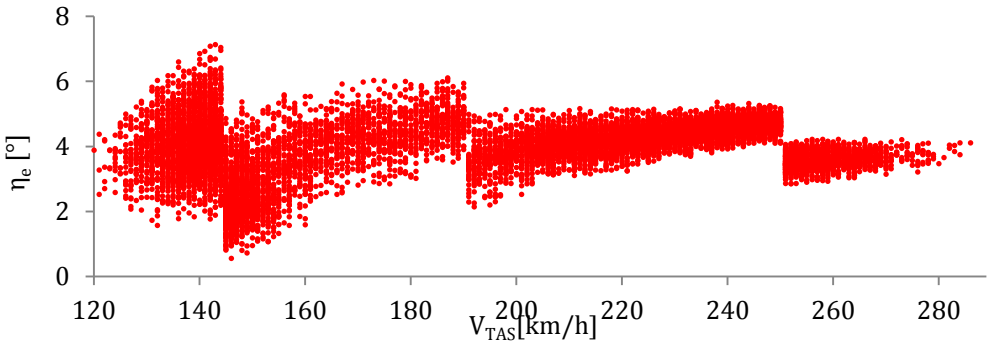

Figure 40: Elevator deflections over the airspeed range of a sample flight

3.6. Summary

This chapter set out to explain the flight analysis procedure. This procedure consisted of the following:

- Extraction of the raw flight data from the IGC files,
- Calculation of total sailplane lift and lift coefficients
- Flight data filtering
- Calculation of wing and horizontal tailplane lift
- Calculation of horizontal tailplane angle of attack and elevator deflection

4. HORIZONTAL TAILPLANE DRAG

With the operating conditions for each flight point known the next step was to calculate the drag the horizontal tailplane creates at each flight point in the flight. Aerodynamic methods are needed to evaluate the lift and drag characteristics of the horizontal tailplane from inputs from the conditions given by the flight analysis calculations. A simplified version of the modified lifting line method developed by Sivells and Neely (1947) was chosen for this purpose.

4.1. Airfoil analysis

The lifting line method that will be used for 3D-analysis of the horizontal tailplane requires viscous 2D airfoil data in order to calculate profile drag. For this reason a reliable and accurate airfoil analysis tool is needed. Xfoil (Drela & Youngren 2001) was chosen as the airfoil analysis code due to the following capabillities:

- Viscous analysis of existing airfoils allow:
    - Forced and free transition
    - Transitional separation bubbles
    - Limited trailing edge separation
    - Lift and drag predictions just beyond the maximum lift coefficient
    - Karman-Tsien compressibility correction
- Drag polar calculation with varying Reynolds numbers

4.1.1. Xfoil validation

Wind tunnel data and co-ordinates for the horizontal tailplane airfoil DU86-137/25 designed by Boermans are given in Boermans and Bennis (1991). This airfoil is used on the ASW-24 Standard Class sailplane and a reduced maximum thickness version of this airfoil is used on the current JS1 horizontal tailplane and will also be used as the airfoil section for this study. This airfoil was designed with the application of artificial transition at 70% chord. This is achieved by placing zig-zag tape on the upper and lower surfaces of the airfoil to eliminate the laminar separation bubble caused by the steep pressure gradient at this location.

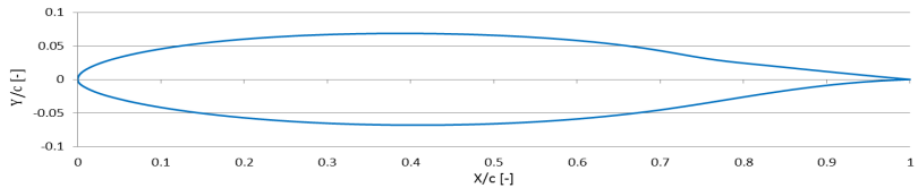

Figure 41: The DU86-137/25 horizontal tailplane airfoil

The wind tunnel tests on the airfoil were conducted in the Low-Speed Low-Turbulence Wind tunnel of Delft University of Technology. Wind tunnel data for elevator deflections of -5° , 0° and 5° at $Re = 0.7 \times 10^6$ were used and compared to Xfoil predictions. The turbulence level in the test section of the wind tunnel varied from 0.018% at 10m/s and 0.043% at 60m/s and Xfoil's e^n factor was adjusted accordingly. The transition location for both the upper and lower surfaces of the airfoil was set to 70% chord.

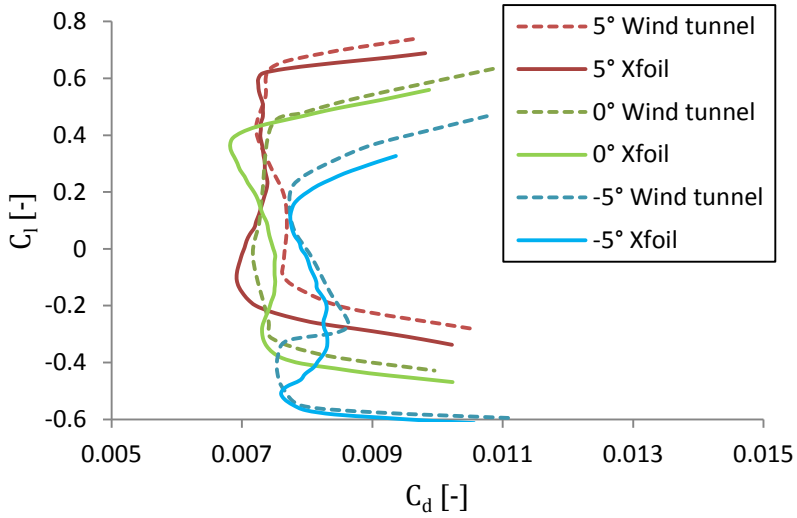

Figure 42: Comparison between wind tunnel tests and Xfoil calculation

Figure 42 shows the comparison of the wind tunnel results from Boermans and Bennis (1991) to the values calculated by Xfoil. A resemblance of the shape of the wind tunnel and Xfoil drag polars can be seen. The results, however, also show that Xfoil has a tendency to under-predict drag which might get worse as the Reynolds number is reduced. The use of Xfoil can be justified due to the comparative nature of

this study where design results will be expressed as differences rather than absolute values. For this reason the error will have small effects on the outcome.

4.2. Modified lifting line method

In order to evaluate lift and drag coefficients a 3D-wing analysis method is required in this study. Sivells and Neely (1947) developed a modified lifting line theory that uses 2D airfoil data to predict profile drag of 3D wings. A simplified version of this method will be used for prediction of horizontal tailplane lift and drag coefficients from the inputs calculated from flights.

4.2.1. Wing parameterisation

As a geometric input the lifting line theory requires chord lengths and their span positions. For this study symmetrical flow is assumed and only half of the wing will be analysed. The wing planform was approximated with trapezoidal sections that will be referred to as the geometrical sections. These geometrical sections can be seen in Figure 43. Each of these sections is described by a section root chord, section tip chord, section span and the airfoils at the root and tip chord positions of each section.

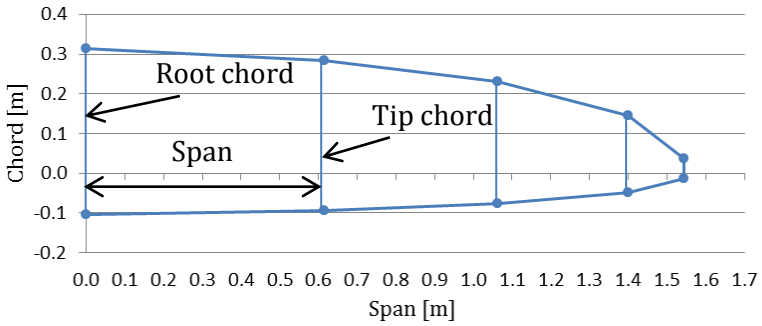

Figure 43: Wing planform parameterization

With the geometrical sections defined the lifting line theory can sub-divide these sections into smaller numerical sections. One important geometrical constraint should be mentioned in the parameterization of specifically the horizontal tailplane. For practicality reasons the hinge line of the elevator should be on a straight line to

ensure that the airfoils hinge location coincides with its design hinge location. This gives the horizontal tailplane a small sweep angle which by definition is not accounted for by the lifting line theory. Due to the small angle, however, the effects of this sweep angle can be neglected.

4.2.2. The numerical model

The lift created by each segment of finite wings does not correspond to the lift predicted by two-dimensional analysis. The lift of each of these sections is strongly influenced by the lift generated by their neighbouring sections. It is thus difficult to analytically predict the lift produced by a given wing geometry. The lifting line theory yields the span-wise lift distribution of a finite wing based on its geometry and flow conditions.

In the lifting line theory the concept of circulation and the Kutta-Joukowski theorem is applied and the unknown effectively becomes the circulation distribution over the span instead of the lift distribution. Through this approach it becomes possible to account for the influence of one section over its neighbours. This influence gives rise to the vertically induced velocity also called up or downwash (w_i) which is related to a change in effective angle of attack over neighbouring sections. This change in angle of attack called the induced angle of attack (α_i) and is the difference between the actual or geometrical angle of attack (α) of a given wing section and its effective angle of attack (α_e).

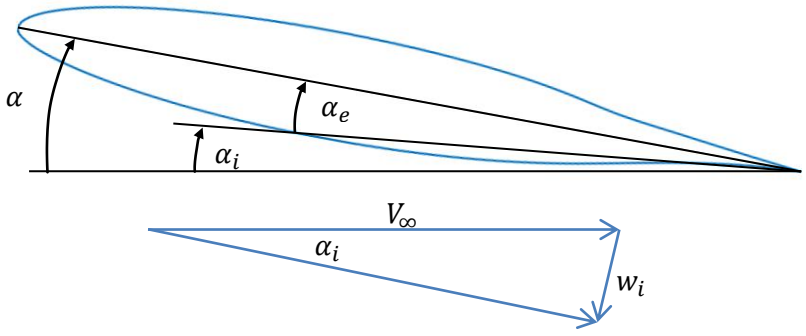

Figure 44: Angle definition for the lifting line theory

In the application of the lifting line theory the wing is divided into N span-wise sections that will be referred to as the numerical sections. It is assumed that the circulation of the wing varies as a function of the location of these sections. This function is assumed to be a Fourier function. The span-wise location y of each chord length that will define the root chord (c_i) of each numerical section is shown in Figure 45.

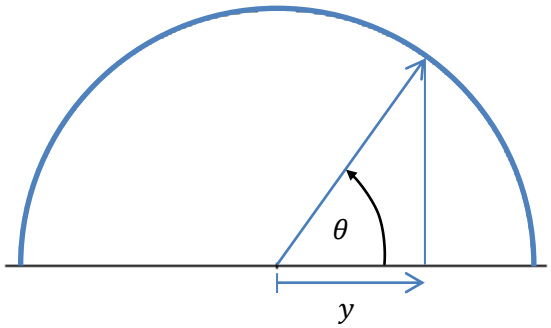

Figure 45: Definition of the span wise location of the numerical sections

This location is given by:

$$y_i = b\cos\theta \tag{4.1}$$

$$where\ \theta = \frac{\pi}{2n}, n = 1\ to\ N \tag{4.2}$$

Where b is the semi-span of the wing. With the locations, and values for c_i known the following system of linear equations can be solved to find the Fourier coefficients A_1 to A_N:

$$\frac{c_i}{8b}\left(C_{l_\alpha}(\alpha - \alpha_0) + C_{l_\eta}\eta\right) = \sum_{n=1}^{N} A_n \sin(n\theta)\left(1 + \frac{nc_i C_{l_\alpha}}{8bsin\theta}\right) \tag{4.3}$$

The values of the angle of attack and elevator lift curve slopes C_{l_α} and C_{l_η} were calculated from the values of C_{l_α} and C_{l_η} of root and tip airfoil of the geometrical section the numerical section is located in.

From the values of the Fourier coefficients A_1 to A_N the section and global lift coefficients can be calculated. Where the section lift coefficient is given by:

$$C_l = \frac{8b}{c_i} \sum_{n=1}^{N} A_n \sin(n\theta) \tag{4.4}$$

And the global lift coefficient by:

$$C_L = \pi A R A_1 \tag{4.5}$$

The induced drag coefficient is also given by a sum of the Fourier coefficients where:

$$C_{D_i} = \pi A R \sum_{n=1}^{N} n A_n^2 \tag{4.6}$$

To calculate the viscous part of the wings drag 2D airfoil data calculated in Xfoil was used. For each numerical section the profile drag coefficient of the root and tip airfoil is needed to calculate its profile drag coefficient. Although it is desirable to calculate each of these drag coefficients separately, it will be more efficient from a coding point of view to use an interpolation scheme to interpolate these values from pre-calculated Xfoil polars. A user-friendly interface for Xfoil is included in XFLR5 (Deperrois 2014) which has the option of batch analyses of airfoils. This option enables the user to rapidly acquire airfoil data at large lists of Reynolds numbers. The effect of the Reynolds number on the drag coefficient becomes more pronounced at lower Reynolds numbers and it is important to choose adequately small Reynolds number increments at which analyses are done. The angle of attack and elevator deflection increments should also be small enough to have no effect on the accuracy of the Xfoil data due to the interpolation process.

The effective angle of attack, α_e, of each numerical section is given by:

$$\alpha_e = \alpha_S - \alpha_i = \alpha_S - \sum_{n=1}^{N} nA_n \frac{\sin(n\theta)}{sin\theta} \quad (4.7)$$

Where α_S is the geometrical angle of attack of the numerical section. From the numerical section effective angle of attack, elevator deflection and Reynolds number the value of the numerical section profile drag coefficient C_{d_p}can be interpolated from the Xfoil polars. The total profile drag coefficient C_{D_p} is then calculated by span-wise integration of the numerical section profile drag coefficients.

The lifting line model described above can thus calculate the total lift coefficient, profile and induced drag coefficients of a given wing. The inputs needed for this model is the geometrical angle of attack, elevator deflection, wing geometry and the ratio of the free stream velocity to kinematic viscosity to calculate the numerical section Reynolds numbers.

4.2.3. Lifting line model validation

Neely *et al.* (1947) conducted wind tunnel tests on several NACA 44-series wings with aspect ratios of 8 10 and 12. The wing with aspect ratio 8 was chosen as a validation case for the lifting line model described above as it falls in the range of suitable horizontal tailplane aspect ratios for sailplanes given by Tomas & Milgram (1999). The characteristics of this wing are given in Table 5.

λ [−]	AR [-]	Airfoils		b [m]	S [m^2]	$\bar{c}$ [m]	Tip twist [°]
		Root	Tip				
2.5	8.040	NACA 4416	NACA 4412	4.572	2.6	0.607	-4.5

Table 5: Lifting line validation wing characteristics

The wind tunnel tests were conducted in the Langley 19-foot pressure wind tunnel. Measurements of lift and drag were made over an angle of attack range of $-4°$ through to the angle of stall. The Reynolds number at the mean aerodynamic chord of the wing for the selected case was 4×10^6. Standard sea-level conditions were assumed and the free stream velocity was calculated as 93.8m/s.

Xfoil polars were calculated for both airfoils for Reynolds numbers of 1.5×10^6 to 6×10^6 with increments of 300000 and angles of attack of $-14°$ to $14°$ with increments of 0.2°. The lift and drag coefficients of the wing were calculated with the lifting line model described above at angles of attack of $-4° \; to \; 12°$ at a free stream velocity of 93.8m/s and standard sea-level conditions.

Figure 46 shows the comparison of the wind tunnel data and the lifting line model. The calculated polar matches the experimental polar well for lift coefficients below 0.6 which make this method ideal for horizontal tailplane design as the maximum lift coefficient of the horizontal tailplane is expected to be below this value for normal flight conditions. For lower speeds under prediction of drag can be expected however, due to the tendency Xfoil has to under predict profile drag.

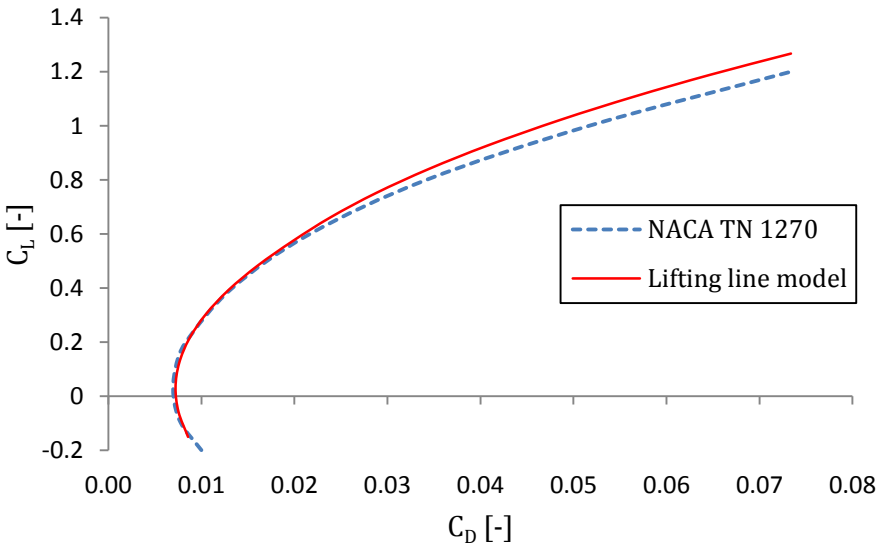

Figure 46: Drag polar comparison of the experimental data and the lifting line method

A comparison of the lift curve predicted by the lifting line model and the experimental data is given in Figure 47. Over-prediction of the zero lift angle of attack can be seen. This results in the under-prediction of lift at angle of attack values lower than 6°. Furthermore, the lift curve slope is over-predicted which can be expected for lower aspect ratio wings.

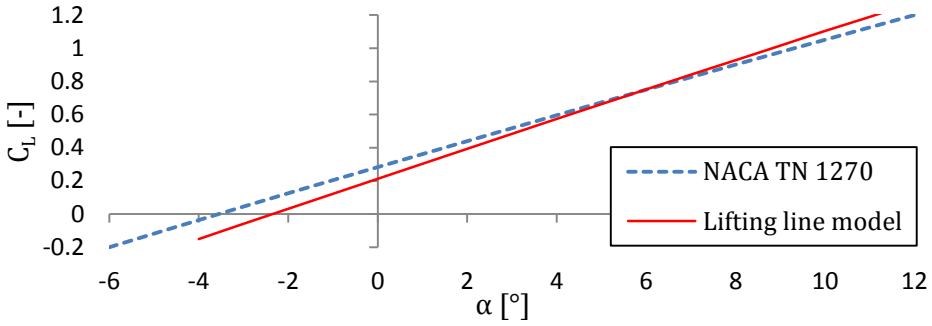

Figure 47: Lift curve comparison of the experimental data and the lifting line method

4.3. Flight point drag calculation

The profile and induced drag coefficients, C_{D_p} and C_{D_i}, were calculated at the angle of attack and elevator deflection calculated with the modified lifting line method described. Xfoil data was constructed for the reduced thickness version of the DU86-137/25 airfoil currently used on the horizontal tailplane of the JS1C. The transition location was set to 70% chord to simulate the artificial transition the airfoil was designed for. The angle of attack range was chosen as $-9°$ to $9°$ with $0.2°$ increments and the elevator deflection range was chosen as $-16°$ to $14°$ with $2°$ increments. The Reynolds number ranges and increments are given in Table 6:

Range	Increment
80000 - 200000	20000
200000 - 500000	50000
500000 - 1000000	100000
1000000 -2000000	200000
2000000 - 3500000	300000

Table 6: Reynolds number ranges for Xfoil polar analysis

The profile and induced drag coefficients were calculated at each flight point's angle of attack and elevator deflection. From the drag coefficient a time based drag value was calculated as follows:

$$\bar{D}_p = qS_H C_{D_p} \Delta t \tag{4.8}$$

$$\bar{D}_i = qS_H C_{D_i} \Delta t \tag{4.9}$$

Where Δt is the time spent at the flight point. Figure 48 shows the time-based profile drag calculated for each point of the sample flight. As expected, a quadratic increase can be seen with an increase in airspeed. This suggests that profile drag reduction at the higher airspeeds will give an advantage.

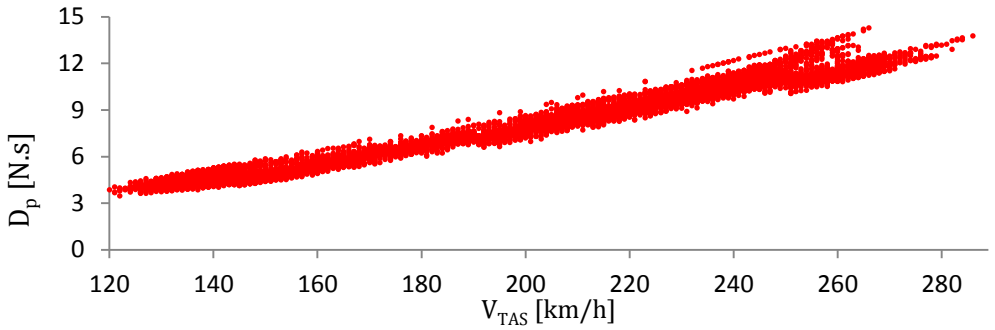

Figure 48: Time-based profile drag calculated for each flight point of a sample flight

Figure 49 shows the time-based induced drag calculated for the sample flight. The induced drag is seen to be low compared to the profile drag with the difference increasing with an increase in airspeed.

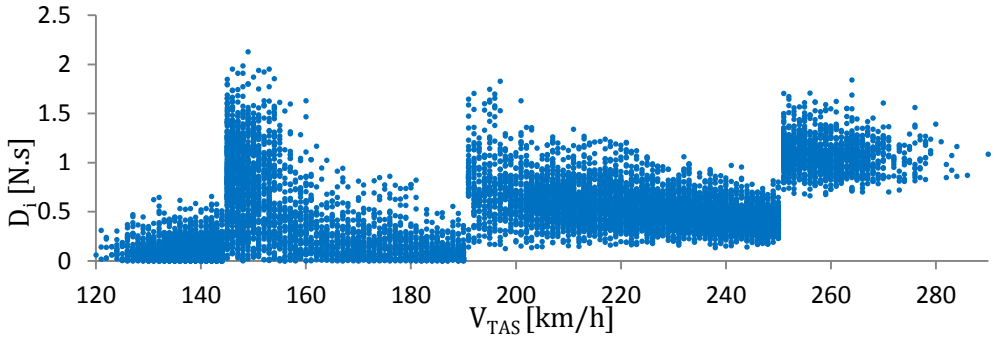

Figure 49: Time-based induced drag calculated for each flight point of a sample flight

Total time-based profile and induced drag was calculated by summing each drag value of the flight. The sum of these values gave the total time-based drag of the horizontal tailplane for the sample flight. Table 7 gives the total time-based induced profile and total flight drag for the sample flight. Profile drag accounts for 93.94% of the total drag again confirming the importance of reduction of profile drag compared to induced drag.

$\overline{D}_{iT}\ [N.s]$	5661.39	6.06%
$\overline{D}_{pT}\ [N.s]$	87749.33	93.94%
$\overline{D}_{T}\ [N.s]$	93410.72	100%

Table 7: Total time-based drag calculated for the sample flight

4.4. Summary

This chapter set out to explain the drag calculation for the horizontal tailplane from the conditions calculated in the flight analysis procedure. This procedure consisted of the following:

- Selection and validation of the airfoil analysis programme Xfoil
- Selection and validation of a 3D wing analysis method
- Calculation of horizontal tailplane profile, induced and total drag for each flight point and total flight drag.

This procedure showed that profile drag is the dominant drag component with 94% of the total flight drag consisting of profile drag. Induced drag accounted for 6% of

total flight drag indicating that the optimisation procedure will be dominated by profile drag reduction.

5. PLANFORM OPTIMISATION

The results of the flight and horizontal tailplane drag analysis procedure give valuable insight into the design space of the horizontal tailplane. Although manual variation of design parameters at this point will also give good results, an optimisation procedure will be far more efficient at producing the best design. For the optimisation procedure design constraints and an objective function needs to be formulated after which an algorithm to minimise the objective function needs to be chosen.

5.1. Optimisation constraints

To ensure design practicality some constraints must be imposed on the optimisation procedure. For this purpose the horizontal tailplane volume and volume coefficient together with the maximum elevator deflections in the manoeuvring and gust envelopes were chosen. Dynamic stability constraints were not imposed as the conventional configuration used is well behaved in regards to dynamic stability (Tomas & Milgram 1999).

5.1.1. Horizontal tailplane volume and volume coefficient

The horizontal tailplane volume gives a relation between the lift curve slope, planform area and tail-arm of the horizontal tailplane which will ensure static stability:

$$V_H = C_{L_{\alpha H}} S_H l_H \tag{5.1}$$

For various practicality reasons a centre of gravity range must be chosen. This range is measured from the wings' aerodynamic centre in an aft direction. The current centre of gravity range for the JS1C 21m variant is 158mm and will thus also be used in this study. This places the aft-most centre of gravity position at 45.5% of the wings mean aerodynamic chord. Sailplanes are typically designed with their aft

centre of gravity limits very close to the neutral point, often within only 5 to 10% of mean aerodynamic chord (Tomas & Milgram 1999). The static margin (SM) was thus chosen as -0.1 which places the aft most centre of gravity position 10% of the mean aerodynamic chord forward of the neutral point. The effective horizontal tail volume needed to give the above-mentioned conditions is given by:

$$\left(\frac{V_H}{V_W}\right)^* = \left(\frac{X_{CG}}{\bar{c}}\right)_{AFT} - SM + 0.25 \tag{5.2}$$

The required horizontal tail volume is given by:

$$V_H = \frac{\bar{c}S_w}{C_{L_\alpha}}\left(\frac{V_H}{V_W}\right)^* \left(1 - \frac{\partial\varepsilon}{\partial\alpha}\right) \tag{5.3}$$

C_{L_α} changes with wing-flap setting and should be calculated for each flap setting and the maximum value should be used as the design value. Table 8 gives the calculated values of V_H required for each flap setting. The maximum value of 18.353 corresponding to the 0° flap setting will be used as the lower horizontal tail volume constraint.

Flap setting [°]	V_H [m³/rad]
-3	17.759
0	18.353
5	18.249
13.5	17.705
20	16.633

Table 8: Required horizontal tail volume for each flap setting

Due to the high percentage drag profile, drag contributes to the total flight drag; the optimisation algorithm is expected to reduce the aspect ratio of the horizontal tailplane. This has a detrimental effect on the lift curve slope of the horizontal tailplane. This constraint will thus ensure an adequate value for $C_{L_{\alpha H}}$ that will still conform to longitudinal static stability requirements.

The horizontal tailplane volume coefficient ($\bar{V}_H$) gives a practical relation between the wing geometry, horizontal tailplane planform area and the tailarm to ensure longitudinal static stability:

$$\bar{V}_H = \frac{S_H l_H}{S_W \bar{c}} \tag{5.4}$$

Through this constraint the optimisation algorithm will be forced to adjust the planform area with changes to the tail-arm. Changes in the mean aerodynamic chord of the horizontal tailplane will result in changes in the tail-arm. A proposed value of 0.5 is given by Raymer (1999) and Howe (2000) for the horizontal tail volume coefficient ($\bar{V}_H$) of sailplanes and will thus be used as the lower horizontal tail volume coefficient constraint.

5.1.2. Manoeuvring and gust envelope

The CS-22 gives airspeed and load factor requirements for compliance through the manoeuvring and gust envelope of a sailplane. Although these envelopes are used for structural design, they give information on the extreme load factor cases expected for a specific sailplane. From these envelopes the maximum lift the horizontal tailplane is expected to produce can be calculated. This will place a constraint on the planform area as the maximum elevator deflection is set at 20° as a result of the airfoil that is used.

The manoeuvring envelope calculated for each flap setting of the JS1-C 21m variant is given in Figure 50. Only positive load factor cases were considered as these will be the extreme cases.

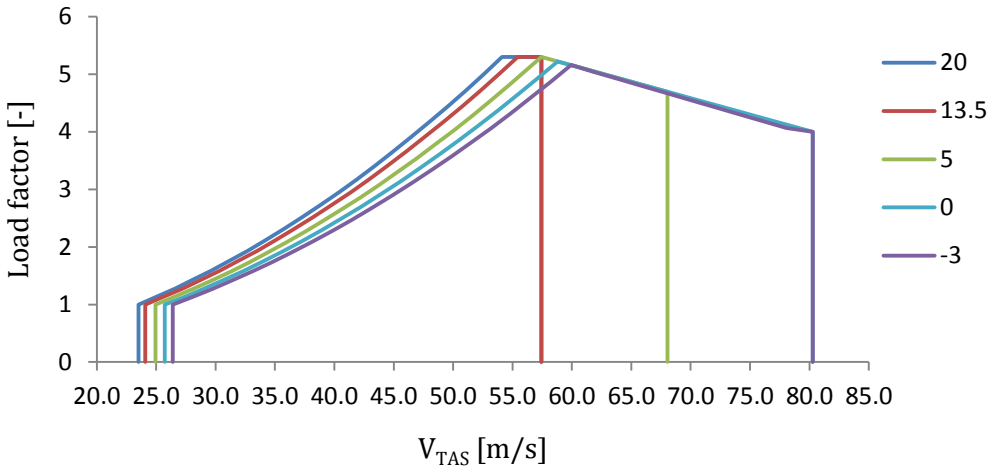

Figure 50: JS1-C 21m manoeuvring envelope

The load factors given by the manoeuvring envelope can be used to calculate the total sailplane lift and with the same method used in sections 3.4 and 3.5 the elevator deflection can be calculated. The elevator deflections calculated for the manoeuvring envelope airspeed range for a sample horizontal tailplane is given in Figure 51. The maximum elevator deflection is seen at the structural design airspeed of the wing in the landing flap setting.

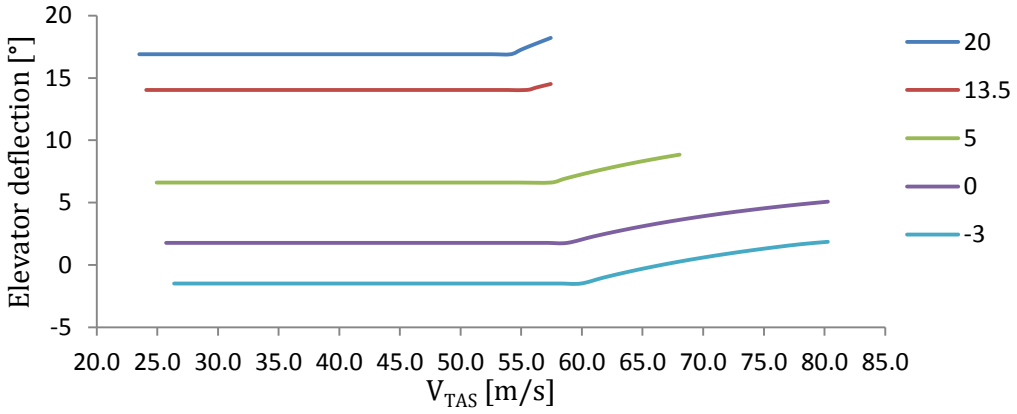

Figure 51: Elevator deflections over the manoeuvring envelope airspeed range

This procedure was repeated for the gust envelope. The gust envelope for the JS1-C 21m variant is given in Figure 52.

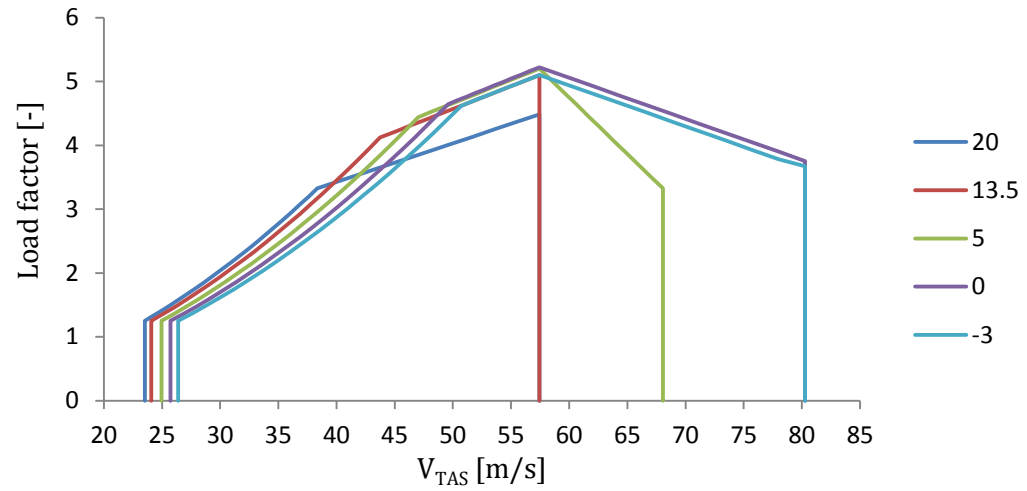

Figure 52: JS1-C 21m gust envelope

The calculated elevator deflections over the gust envelope airspeed range are given in Figure 53. The maximum elevator deflection can again be seen at the structural design airspeed of the wing in the landing flap setting.

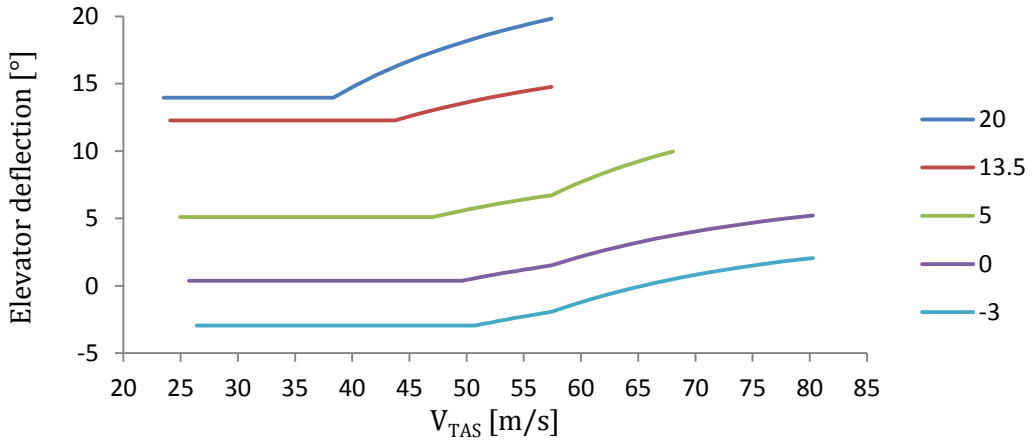

Figure 53: Elevator deflections over the gust envelope airspeed range

5.1.3. Other constraints

The fuselage length between the leading edge of the wing and trailing edge of the horizontal tailplane is fixed. This length should thus be constrained to stop the optimisation algorithm from increasing the tail length as this will give drag

reductions due to the fact that no calculation is done on the increased tail boom area and thus tail boom drag that will accompany this.

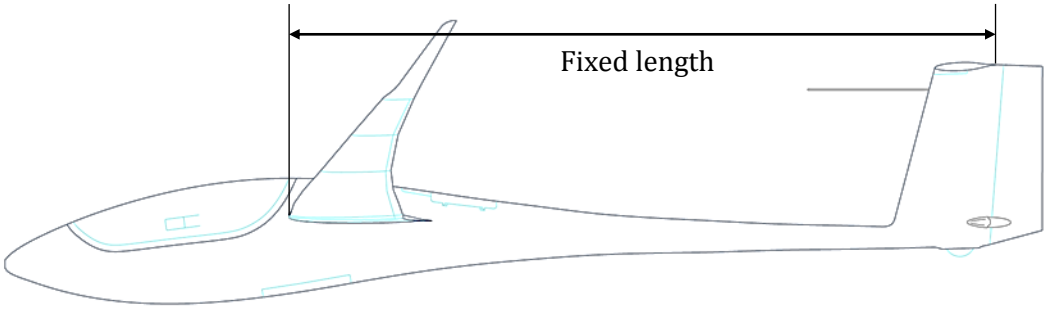

Figure 54: Tail length constraint

Due to the inaccuracy of the lifting line model at aspect ratios lower than 4 (Rathakrishnan 2013) a lower aspect ratio constraint of 6 was chosen to ensure accurate lift and thus horizontal tailplane angle of attack and elevator deflection predictions.

5.2. The objective function

For successful planform optimisation an objective function representative of the flight conditions found in flights should be formulated. As the aim of this study is the aerodynamic optimisation of the horizontal tailplane, minimisation of the total drag over various flights needs to be done. This comes with an impractical computational expense due to the large number of flight points that will accompany the use of multiple flights. This is mostly due to the aerodynamic coefficient calculations, which shows the need for a computationally inexpensive aerodynamic analysis method.

The use of only one flight, however, can give biased results due to weather conditions and pilot flight preferences. It was thus decided to introduce weights calculated for each airspeed from different flights into the calculation of total flight drag and to impose these weights on one flight that will be used as the optimisation flight. For the calculation of the airspeed weights six flights, all filtered with the method given in section 3.3, representing 120000 flight points were used. From

these six flights the overall percentage of time spent at a particular airspeed was calculated. The calculated airspeed weights are shown in Figure 55.

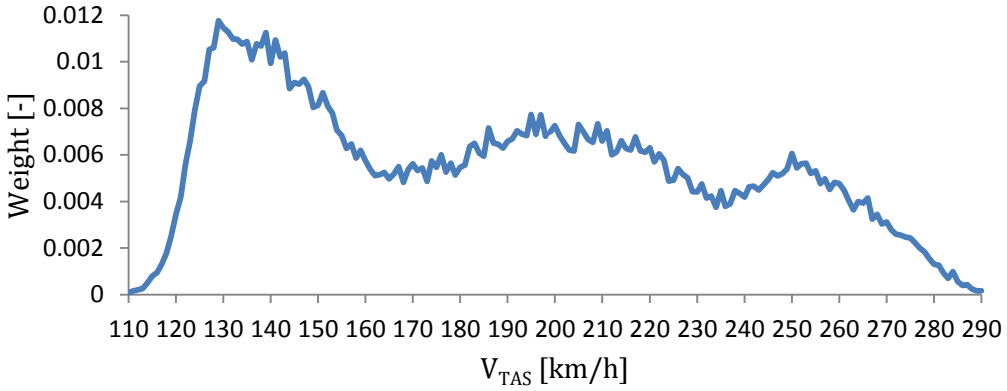

Figure 55: Airspeed weights

The total time-based drag for each airspeed was calculated by summing the time-based drag of each flight point at the corresponding airspeed for the optimisation flight, and multiplied with the corresponding airspeed weight. This produced a weighted drag value for each airspeed. As an example consider $V_{TAS} = 149\ km/h$ for a sample flight. The total time based drag for this airspeed is given by:

$$\overline{D}_{149} = \sum_{V_{TAS} = 149\ km/h} (\overline{D}_p + \overline{D}_i) = 718\ N.s \qquad (5.5)$$

The total weighted time-base drag for this airspeed is then given by:

$$\overline{D}_{\omega 149} = 100(\omega_{149}\overline{D}_{149}) = 577\ N.s \qquad (5.6)$$

Where ω_{149} is the airspeed weight of $V_{TAS} = 149\ km/h$. Figure 56 shows the weighted and unweighted drag for each airspeed in a sample flight. For this specific flight a disproportionate amount of time-based drag can be seen in the higher airspeeds. This shows the need for the airspeed weights to ensure the optimisation results won't be biased towards the optimisation flight.

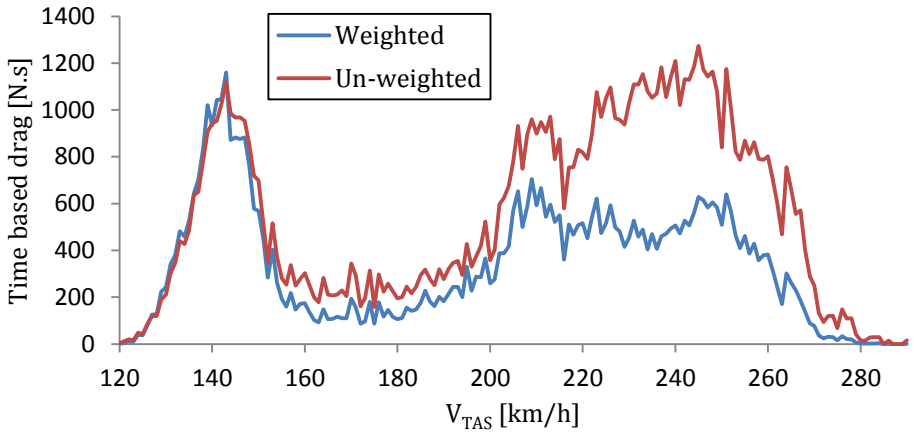

Figure 56: Weighted and un-weighted time based drag for a sample flight

The airspeed weighted drag values were summed over the flight speed range to give the total weighted drag for the optimisation flight and also the value of the objective function for the horizontal tailplane analysed.

5.3. The optimisation algorithm

An optimisation algorithm needs to be chosen and will be used to minimize the objective function under the given constraints. Various optimisation software packages are available and coding an optimisation algorithm will thus be unnecessary.

The Basic Solver in Excel includes constrained linear and non-linear optimisation algorithms that are able to handle up to 200 variables and 100 constraints. Due to the availability of Microsoft Excel and its relatively low cost all the procedures described in sections 3 and 5 and the lifting line model were coded in Visual Basic and the constrained optimisation of the objective function was handled by the Basic Solver.

Due to the non-linearity of the problem posed by this study a non-linear algorithm needs to be implemented. The Basic Solver includes two algorithms that can be used for constrained non-linear optimisation; a gradient-based local algorithm and an evolutionary global algorithm. Due to the relatively higher computational expense expected of a global algorithm, the local gradient algorithm will be used. This

gradient method uses the generalised reduced gradient (GRG) algorithm as implemented by Lasdon *et al.* (1978) in the GRG2 code. The generalised reduced gradient algorithm is a non-linear extension of the simplex method which have shown to be efficient and robust (Lasdon *et al.* 1978).

5.4. The optimisation procedure

Integration of the formulated constraints, objective function and chosen optimisation algorithm was the next objective. The optimisation algorithm is connected to the objective function through design variables. The overall objective was to minimize the objective function, i.e. the total weighted drag created by the horizontal tailplane in the optimisation flight subject to the constraints discussed. The planform shape given in Figure 56 was used as the starting geometry for the optimisation procedure. The five chord positions (1-5) and the area of each of the four sections (6-8) shown in Figure 56 were chosen as the design variables. The general reduced gradient algorithm needs input values or first guesses to start the optimisation routine. A baseline horizontal tailplane was chosen as the initial geometrical input. This horizontal tailplane consists of four tapered sections, has a semi-span of 1.534m and a planform area of $1m^2$. The tip section of the baseline horizontal tailplane was adapted to be represented by only one section and the elevator was changed to a full span elevator. Through this the optimisation algorithm is able to vary the design variables and assess the impact of each change on the objective function.

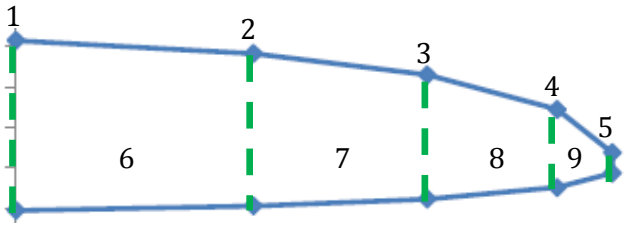

Figure 57: Optimisation spreadsheet layout

A summary of the optimisation constraint values are given in Table 9. The constraint on the distance between the leading edge of the wing and trailing edge of the horizontal tailplane was not given explicitly but rather used in the calculation of the

tail arm. Other functional constraints were added to ensure that all design variables are kept positive and non-zero. The tip chord of each geometrical section was also constrained to be smaller or equal to the root chord of the section.

Constraint	Value
V_H [m³/rad]	> 18.35
$\bar{V}_H$ [-]	> 0.5
η_{MEmax} [°]	< 20
η_{GEmax} [°]	< 20
AR_H [-]	> 6

Table 9: Optimisation constraints summary

The solver setup parameters window is shown in Figure 58. The optimisation routine was executed three times in total. For the first execution the number of numerical sections given as an input to the lifting line model was set to ten. After a converged solution was found by the Basic Solver the solution was saved and the numerical section count was increased to fifteen. In this way the size of the design space was reduced for the execution with increased numerical section count which reduced the time needed to give a converged solution. This procedure was repeated once more with 20 numerical sections at which point the change in the planform shape did not change significantly compared to the fifteen numerical section solution.

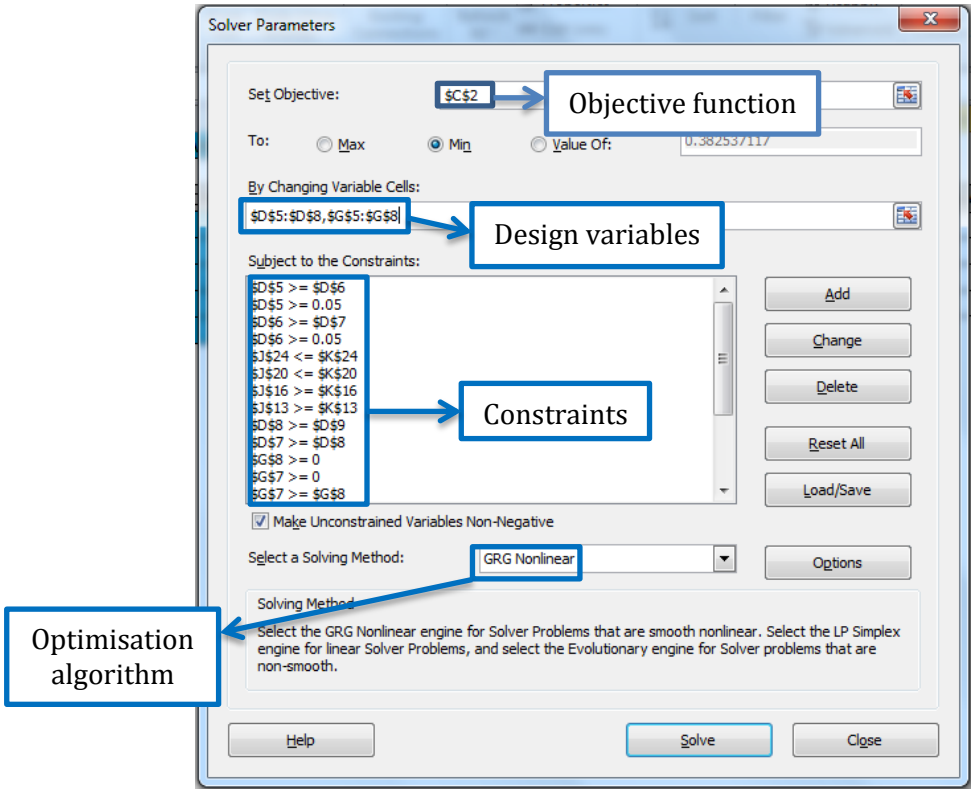

Figure 58: Solver setup

5.5. Planform optimisation results

The baseline and optimised semi span planform shape are given in Figure 59. In total the optimisation procedure of three executions took close to eighteen hours of run time. This again showed the necessity of a simple aerodynamic model for this study. The lifting line model enabled faster calculations due to the relatively small matrices that need to be solved compared to the other models discussed.

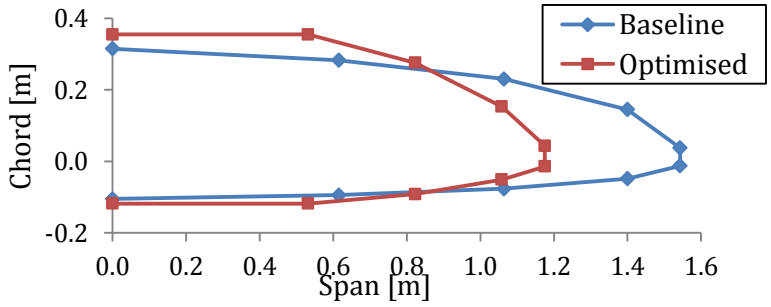

Figure 59: Planform optimisation results

Table 10 gives a comparison of the important parameters of the baseline and optimised horizontal tailplanes. An appreciable decrease in both planform area and span can be seen. This results in a large decrease in aspect ratio which was expected as the baseline horizontal tailplane aspect ratio fell outside the range of 5 to 8 given by Tomas & Milgram (1999). Although the minimum aspect ratio constraint was set to six it is seen that this value did not reach the constraint value which suggests that an aspect ratio of six is close to the optimum for the JS1-C 21m variant. Both stability constraints i.e. the tail volume and tail volume coefficient are seen to have been reached. This forced the optimisation algorithm to find the optimum ratio of planform area to lift the curve slope which could be the reason why the aspect ratio was not reduced to the constrained value. Increases in the maximum elevator deflection for the manoeuvring and gust envelopes can be seen which is expected due to the decrease in planform area. A decrease of 14.31% in total weighted drag is seen compared to the baseline horizontal tailplane.

	Baseline	Optimised	% Change
S_H [m^2]	1.000	0.914	-8.60%
b_H [m]	3.086	2.35	-23.85%
AR_H [-]	9.523	6.042	-36.55%
V_H [m^3/rad]	22.444	18.353	-18.23%
$\bar{V}_H$ [-]	0.554	0.500	-9.75%
η_{MEmax} [°]	13.46	16.89	25.48%
η_{GEmax} [°]	15.47	18.69	20.81%
TWD $[N.s]$	109070.32	93464.00	-14.31%

Table 10: Comparison of important parameters of the optimised and baseline horizontal tailplanes

5.6. Verification method

Although the results of the lifting line model are in good agreement with experimental data, the model gives no insight into the flow at the wing tips. For this reason a CFD flow solver is needed for the design of the horizontal tailplane tips and verification of the final design. The CFD package STAR-CCM+ was chosen as it was

used successfully by Hansen (2014) to simulate the performance of the Standard Cirrus sailplane.

5.6.1. The turbulence model

Menter (1994) combined the best of the previously developed $k-\varepsilon$ and $k-\omega$ turbulence models into the $k-\omega\ SST$ (Shear Stress Transport) turbulence model. In this hybrid model the standard $k-\omega$ model is used in the inner region of the boundary layer and the standard $k-\varepsilon$ model in the outer regions of the free-shear flows.

5.6.2. The transition model

Due to the presence of laminar separation bubbles in horizontal tailplane flows, accurate prediction of transition is of the utmost importance. The $\gamma - Re_\theta$ transition model was chosen to predict the transition location. This model is a correlation based transition model that solves two extra transport equations, one for intermittency (γ), and one for the local transition onset momentum thickness Reynolds number, Re_{θ_t}. Where the local momentum thickness Reynolds number, Re_{θ_t}, is related to the critical value, Re_{θ_c}, and intermittency production is switched on when Re_θ is larger than the local critical value.

The only input the model requires is the definition of the Re_{θ_t} correlation defined in the free-stream. This definition ensures that the Re_{θ_t} correlation takes the value of 1 in the free-stream, and 0 inside the boundary layer. The mesh requirements for using the Re_θ transition model are high quality, refined low Reynolds number mesh. The distance from the wall boundary to the first cell centroid in the mesh determines how the boundary layer is resolved by the turbulence model. To enable the $\gamma - Re_\theta$ transition model to converge, the y^+ values need to be in the region 0.1 to 1 (Hansen 2014), and have a growth rate and stream-wise mesh spacing in the transition area fine enough to capture the laminar separation bubble.

5.6.3. CFD validation

The wind tunnel data given by Neely *et al.* (1947) was again used for validation purposes for the models used and the flow conditions and wing geometry is the same as those used in the lifting line method validation. The flow domain setup is shown in Figure 60. The dimensions of the flow domain were chosen in relation to the test wing's root chord and semi span.

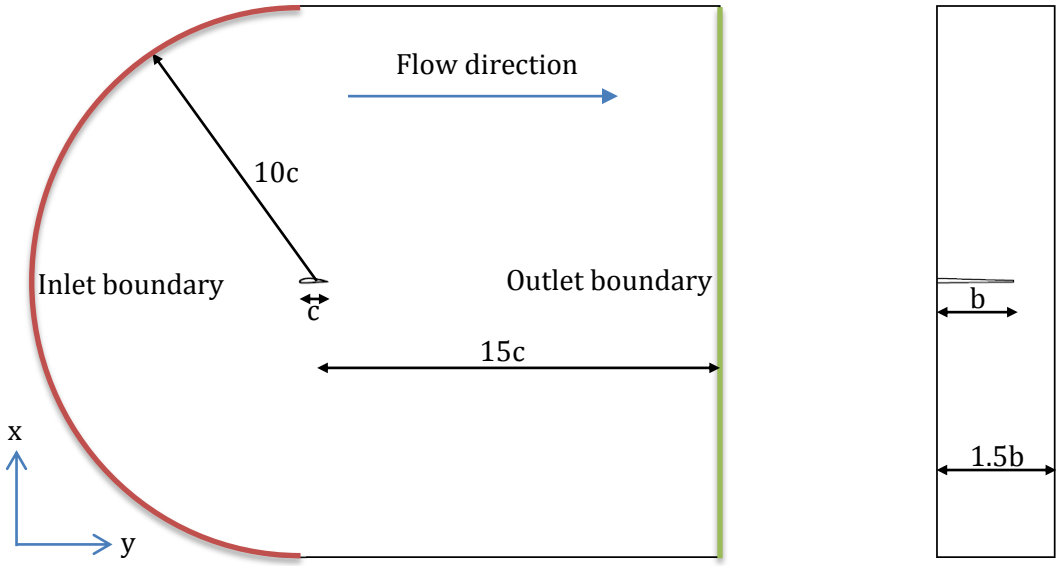

Figure 60: CFD validation flow domain

The flow domain was meshed with cubical cells called trimmer cells. A prism layer consisting of 20 layers were placed on all wing surfaces except the trailing edge. A wake and tip vortex refinement volume were placed over the wing starting from 50mm upstream of the root chord's leading edge to 2m downstream of the root chord trailing edge.

For the mesh independency study the wings angle of attack was set to 6°. The surface size of the cells on the wings surface was set to a value that ensured a y^+ value in the 0.1 to 1 range. The cell size of the wake refinement volumes was given as values for the x, y and z size and varied in subsequent simulations to evaluate the effect of the mesh cell count on the lift and drag coefficients of the wing.

Figure 61 shows the influence of the mesh cell count on the predicted drag coefficient. A decrease in the predicted value can be seen. As the wake refinement cell size was reduced to increase the cell count the importance of a well refined wake region can be seen. From a cell count of 23 million upward the change in the drag coefficient value predicted with cell count increase is in the 6th decimal and is sufficiently small to assume convergence.

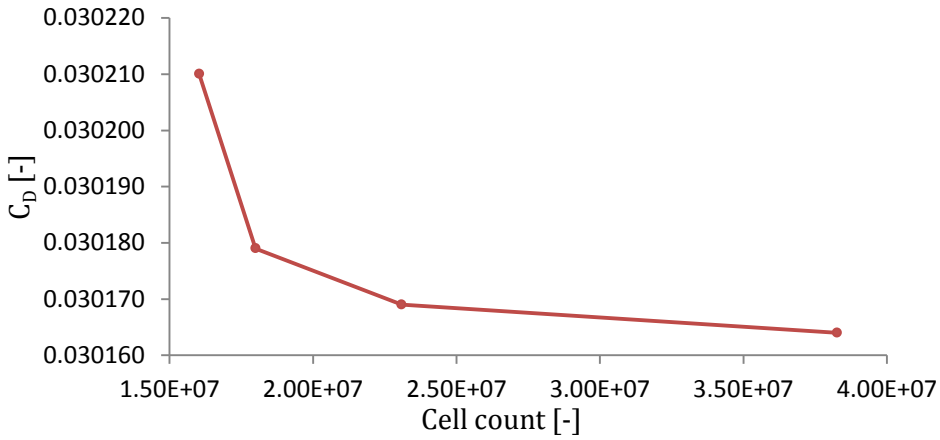

Figure 61: Effect of mesh density on predicted drag coefficient

Figure 62 shows the influence of the mesh cell count on the predicted lift coefficient. The same trend seen in the case of the drag coefficient can be seen where the change in lift coefficient is seen to become sufficiently small from a cell count of 23 million. The mesh values of this simulation were used for the subsequent evaluations.

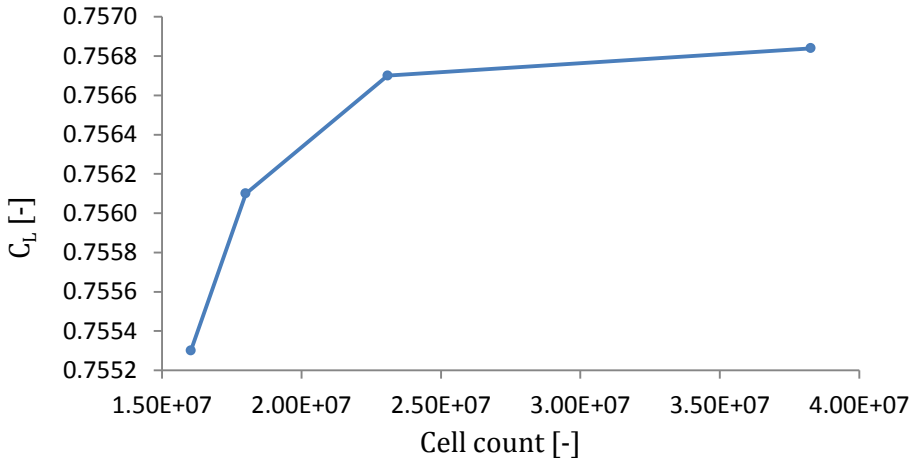

Figure 62: Effect of mesh density on predicted lift coefficient

Five simulations were conducted at angles of attack of $-6°$, $-3°$, $0°$, $6°$ and $12°$ with the same free stream conditions used in the lifting line model validation. The mesh values from the mesh independency study were used to mesh each flow domain. Figure 63 shows the comparison of the simulation results of each angle of attack with the experimental data in Neely *et al.* (1947). In the lift coefficient range the horizontal tailplane is expected to operate, an over-prediction of the drag coefficient is seen. The shape of the drag polar is captured well and drag increments with increases or decreases in the lift coefficient can thus be expected to be accurate.

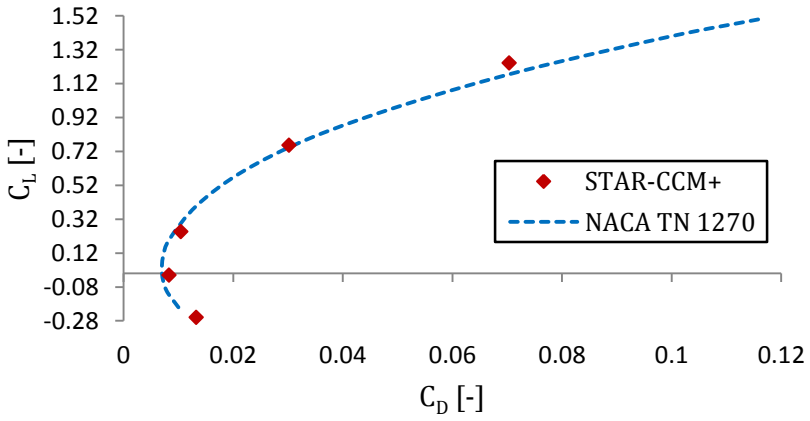

Figure 63: Drag polar comparison of the experimental data and CFD results

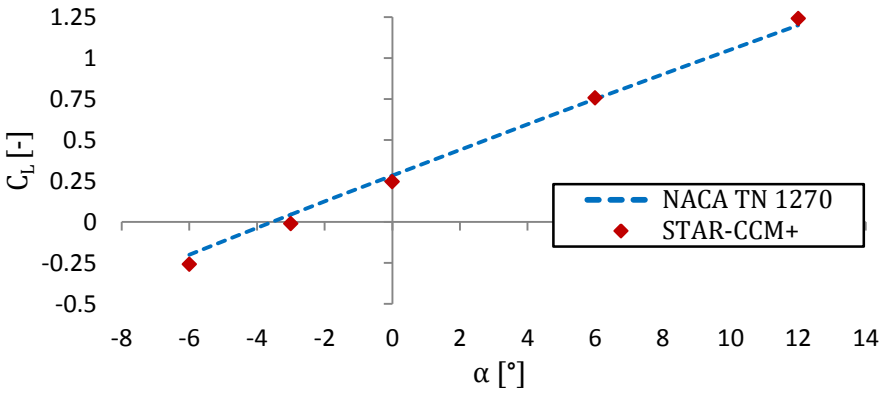

Figure 64: Lift curve comparison of the experimental data and CFD results

5.7. Planform optimisation verification

Spot checks with CFD were chosen to verify the results of the optimisation procedure as it will be impractical to verify the calculations done for each flight point. Two flight points were chosen for this purpose the first where the biggest time-based drag reduction was found and the second where the baseline horizontal tailplane showed to be better than the optimised. Table 11 gives the flow and horizontal tailplane angle parameters for the maximum time-based drag reduction case.

	Baseline	Optimised
V [km/h]	249	249
ρ [kg/m³]	1.066	1.066
ν [m²/s]	1.64E-05	1.64E-05
μ [Pa.s]	1.75E-05	1.75E-05
α_H [°]	-2.892	-2.892
η_e [°]	4.960	5.127

Table 11: Parameters for the maximum time based drag reduction case

	Baseline	Optimised
V [km/h]	149	149
ρ [kg/m^3]	0.862	0.862
ν [m^2/s]	1.95E-05	1.95E-05
μ [Pa.s]	1.68E-05	1.68E-05
α_H [°]	2.313	2.313
η_e [°]	0.999	2.271

Table 12: Parameters for the minimum time based drag reduction case

5.7.1. Verification flow domain and mesh setup

The flow domain dimensions were chosen in the same way as illustrated in Figure 60. For wake refinement a block was placed over the wing. This block started 0.05m from the root leading edge and extended 2m downstream. The thickness of the block was chosen as 0.1m below the lowest point on the wing surface and 0.1m above the highest point. The width of the block was chosen as 1.2 times the semi-span of the wing. The whole refinement block was rotated about the hinge line of the wing to match the angle of flow is expected due to the downwash behind the wing.

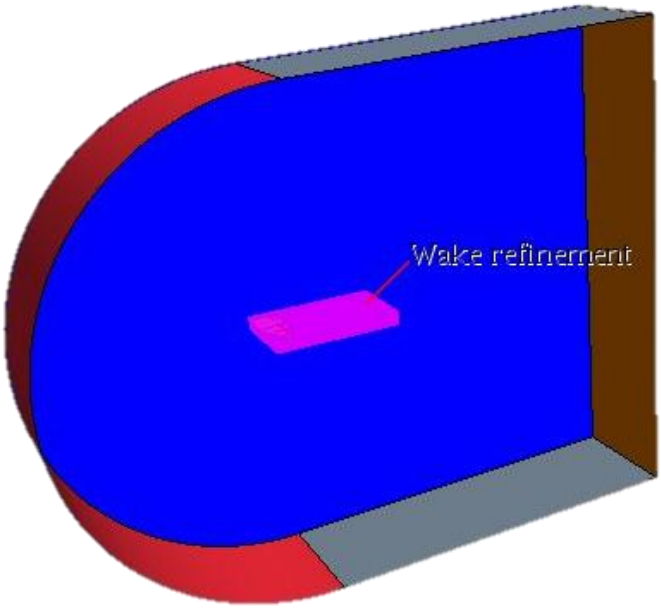

Figure 65: Verification flow domain setup

The wing surface was meshed with cells of target size of 3mm and a minimum size of 0.1mm to ensure refinement of the leading and trailing edges. A non-zero trailing edge meshed with 0.1mm surface size cells was used to ensure adequate cell refinement. The wing was wrapped with fifteen prism layers where the thickness of the first layer adjacent to the wing surface was chosen to ensure a y^+ value of less than 1. The rest of the flow domain was meshed with trimmer cells with a growth rate of 1.1 to give adequate mesh refinement in the volume around the wake refinement block. The wake refinement block was meshed with anisotropic trimmer cells with an x size of 6mm and y and z size of 4mm. The mesh values were kept the same for all four simulations to ensure that mesh density have no influence on the comparisons.

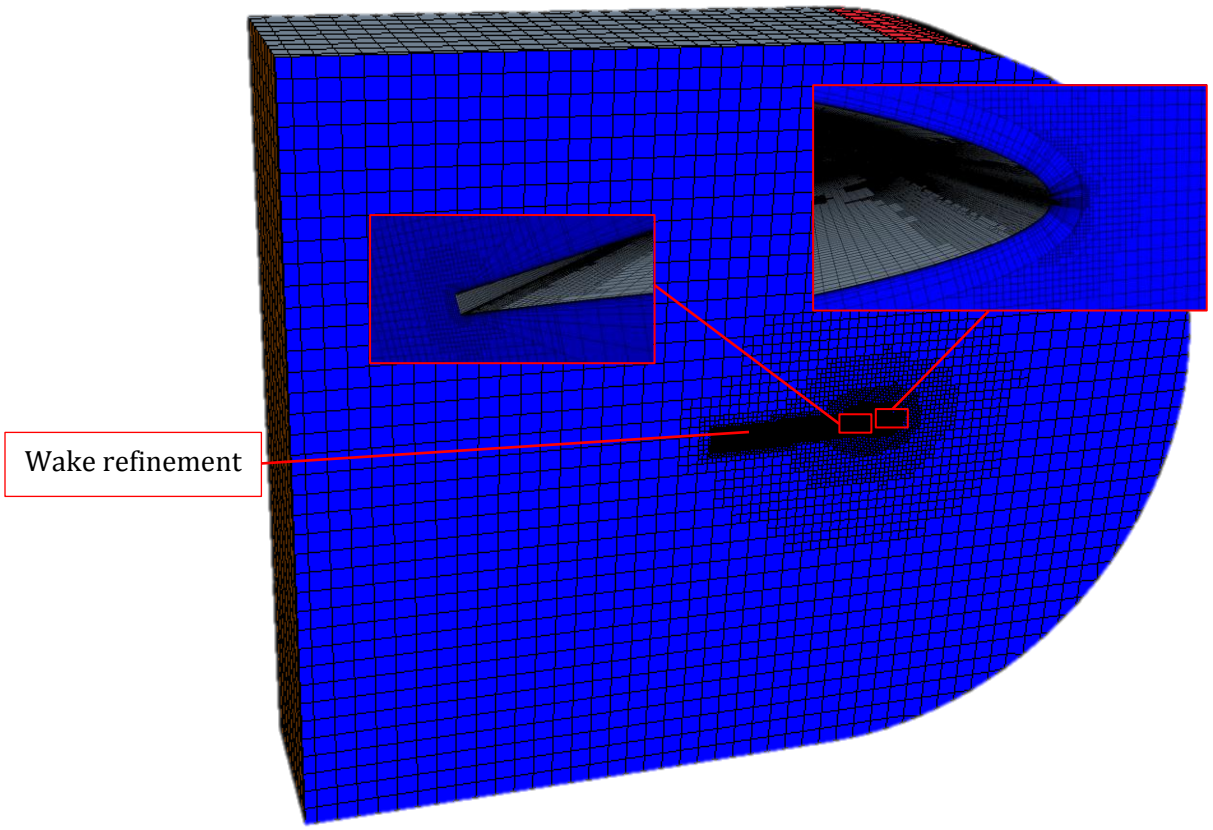

Figure 66: Verification mesh setup

5.7.2. Solver setup and results

The $k-\omega\ SST$ turbulence model coupled with the $\gamma - Re_\theta$ transition model was again used in all four simulations. The flow parameters and horizontal tailplane angles given in Table 11 and Table 12 were used. The C_L, C_D and ΔC_D values calculated in the optimisation procedure and those given by the CFD simulations were compared where the ΔC_D is the most important as it will show if the predicted drag reductions were accurate. Forced transition was not applied in the CFD simulations which are expected to over predict profile drag due to a presence of separation bubbles due to natural transition.

Table 13 gives the results of the minimum time drag difference. A difference of -2.85% is seen for the calculated and CFD simulation for the baseline horizontal

tailplane and -1.49% for the optimised horizontal tailplanes lift coefficients. This indicates a slight over-prediction of lift by the lifting line model which was also seen in the CFD validation. Although this resulted in under-prediction of the elevator deflection angle the drag difference expected will be very small. A difference of 9.65% can be seen between the drag coefficient calculated in the optimisation procedure and the simulation value for the baseline horizontal tailplane. For the optimised horizontal tailplane a difference of 9.94% is seen indicating an under-prediction of the drag coefficient in the optimisation procedure which can be expected as forced transition was not used in the simulations. The 2.49% difference between the calculated drag coefficient difference calculated and that given by the simulations, show under-prediction by the optimisation procedure suggesting that the total weighted drag reduction of 14.31% compared to the baseline horizontal tailplane may be larger.

	Calculated		Star-CCM+	
	Baseline	Optimised	Baseline	Optimised
C_L [-]	0.03795	0.04172	0.03687	0.04110
C_D [-]	0.00515	0.00489	0.00570	0.00543
ΔC_D [-]		-2.616E-04		-2.683E-04

Table 13: Maximum time-drag difference verification case results

Table 14 gives the results for the minimum time-drag reduction case. For the lift coefficients the same trend is seen as in the maximum case with a baseline horizontal tailplane difference of -1.29% and optimised horizontal tailplane difference of -0.179% in calculated and predicted lift coefficients. This again shows over-prediction of lift coefficients by the lifting line method and thus a small under-prediction of elevator deflection. Under prediction of the drag coefficient is seen in the baseline horizontal tailplane case with the simulation results 5.31% larger than the calculated value. For the optimised horizontal tailplane case a small over-prediction of drag is seen with the calculated value 0.6% larger than the value given by the CFD simulation. Over-prediction of the drag coefficient difference is again seen for the calculated value compared to that of the simulation, which again suggests the total weighted drag-reduction percentage could be larger.

	Calculated		Star-CCM+	
	Baseline	Optimised	Baseline	Optimised
C_L [-]	0.2894	0.3182	0.28565	0.31763
C_D [-]	0.00976	0.01240	0.010339	0.012326
ΔC_D [-]		2.634E-03		1.987E-03

Table 14: Minimum time-drag reduction verification case results

5.8. Planform performance evaluation

For the purpose of performance evaluation a flight not used in the optimisation procedure was chosen. The drag calculations given in section 4 were repeated for both the baseline and optimised horizontal tailplanes. To compare the performance improvement of the optimised horizontal tailplane, the values calculated for the optimised horizontal tailplane were then subtracted from those of the baseline to give the time-based drag reductions for induced, profile and total drag. The reduction in time-based induced drag for each flight point is given in Figure 67. An overall increase in induced drag is seen which can be expected due to the reduction in the span of the optimised horizontal tailplane.

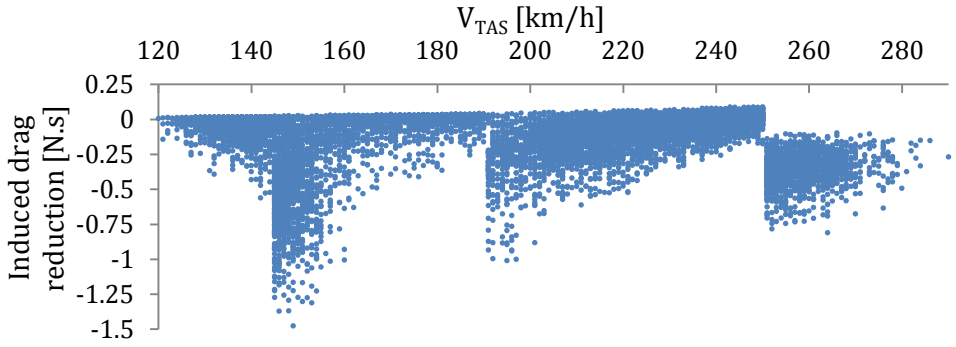

Figure 67: Time-based induce drag reduction for each flight point of the performance evaluation flight

Figure 68 gives the calculated time based profile drag reduction for each flight point of the performance evaluation flight. Decreases in profile drag can be seen in all

flight points which again show the importance of profile drag reduction in horizontal tailplane design.

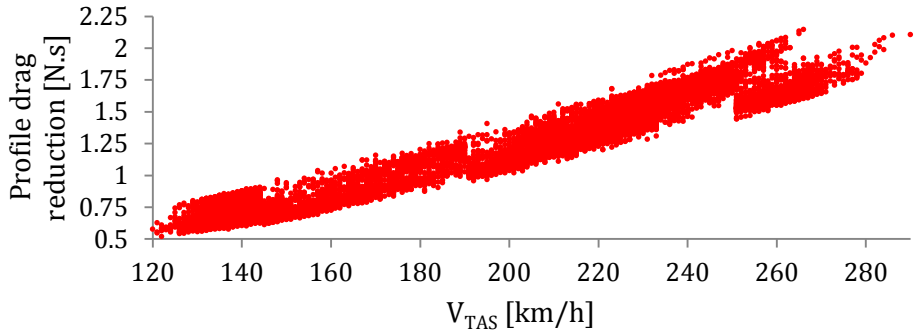

Figure 68: Time-based profile drag-reduction for each flight point of the performance evaluation flight

The time-based total drag reduction for each flight point of the performance evaluation flight is given in Figure 69. Drag reductions are seen for the majority of flight points except for two airspeed intervals where a portion of the flight points showed an increase in drag.

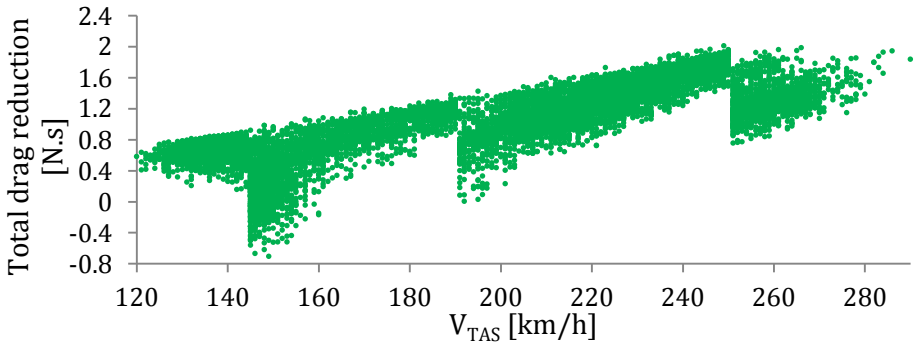

Figure 69: Time-based total drag-reduction for each flight point of the performance evaluation flight

Table 15 shows the comparison of the total flight drag and its components. An increase of 20.4% is seen in induced drag that is expected due to the decrease in span of the optimised horizontal tailplane compared to the baseline. A decrease of 16.3% in profile drag is seen together with a decrease in total flight drag of 14.1%. This shows the small influence a seemingly large increase in induced drag has on the

total flight drag. The optimisation drag reduction of 14.31% compares well to the drag reduction shown in the performance evaluation flight. It can however be expected that some flights will not reflect this.

	Baseline	Optimised	Reduction
Induced drag	5661.39	6815.839	-20.4%
Profile drag	87749.3	73430.18	16.3%
Total drag	93410.7	80246.02	14.1%

Table 15: Comparison of flight drag

5.9. Summary

This chapter set out to explain and discuss the planform optimisation procedure. Firstly, optimisation constraints were formulated; these constraints consisted of lower constraint values for the horizontal tailplane volume and volume coefficient to ensure longitudinal stability. Upper constraints were imposed on the maximum elevator deflection found in the manoeuvring and gust envelopes specified by the CS 22 together with some practicality constraints.

An objective function was formulated consisting of the drag created by the horizontal tailplane in a flight subjected to airspeed weights calculated from other flights. The generalised reduced gradient non-linear optimisation algorithm implemented in Excel's Solver add-in was used to minimise the objective function subject to the constraints formulated.

The results of the optimisation procedure show a 14.3% decrease in flight drag compared to the baseline horizontal tailplane used. These results were verified by simulating both the optimised and baseline horizontal tailplane at two flight points with CFD and comparing the simulation results with the calculations done for these points in the optimisation procedure.

A performance evaluation was also conducted where the optimised and baseline horizontal tailplanes were put through a flight not used in the optimisation

procedure. The performance evaluation showed a decrease of 14.1% in total flight drag which show that the use of airspeed weights and only one flight didn't produce biased results towards the optimisation flight.

6. TIP DESIGN

Hoerner (1965) showed that reductions in both profile and induced drag are possible with some tip shapes. As CFD will be used for this design multi-point optimisation will not be conducted on the tip shapes, one or more flight points were chosen to make design decisions in regards to what tip shape will suit the optimised planform. The first investigation was conducted on the ratio of elevator span to horizontal tailplane span as this is expected to have an effect of tip performance. For the second investigation the best elevator to span ratio was incorporated into a tip shape given by Hoerner (1965) which suited the operating spectrum of the planform.

6.1. Elevator span to horizontal tailplane span ratio

All simulations used for the elevator span ratio were conducted with the same mesh values discussed in section 5.7.1. The two flight points, given in Table 11 (point 1) and Table 12 (point 2), used in the verification of the planform optimisation procedure was again used. In total six simulations were performed - three for the flight point where maximum drag reduction was encountered and three for the point showing a drag increase. Figure 70 shows the three elevator span ratios that were investigated.

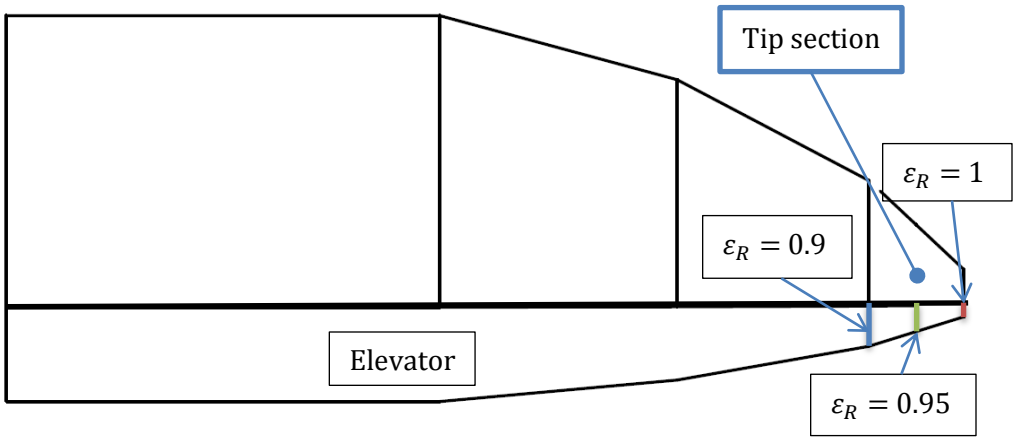

Figure 70: Elevator span description

The results for point 1 are given in Figure 71.

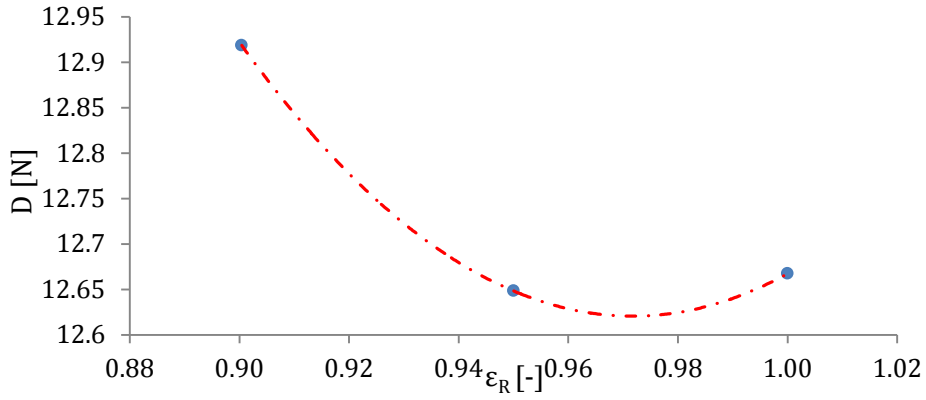

Figure 71: Elevator span ratio investigation results for point 1

By applying a second order polynomial curve fitting the best elevator span ratio is seen at 0.97 for point 1. It can be assumed that profile drag will make up the largest portion of the drag at this point due to the low lift coefficient. Figure 72 shows constrained streamlines on the surface of the tip sections of the elevator span ratios investigated. The laminar separation bubble on the tip section can be seen to decrease with a decrease in elevator span ratio. This also indicates that forced transition should also be implemented on the tip section as it was not employed in the baseline horizontal tailplane. Due to the decrease in elevator area with a decrease in span ratio, higher elevator deflections are seen for the $\varepsilon_R = 0.9$ and 0.95 cases which in turn will increase the profile drag of the inner wing sections which limits the decrease in elevator span ratio.

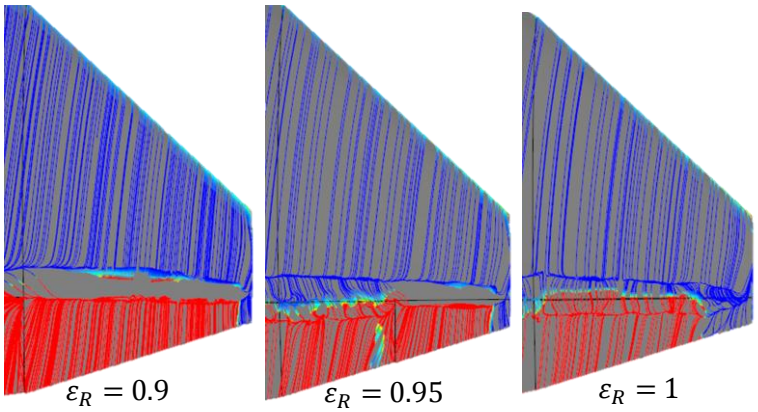

Figure 72: Tip surface flow patterns for point 1

The results for point 2 are given in Figure 73. Here the opposite of that seen for point 1 is observed. This is mostly due to the larger influence of induced drag due to the higher lift coefficient. Although small changes to the vortex span are seen, the addition of a second vortex (see Figure 75) due to the sudden decrease in the span wise local lift coefficient where the elevator ends in the span-wise direction. The addition of the second vortex seems to be advantageous at higher lift coefficients. The best elevator span ratio for point 2 is 0.93 which is lower than the best ratio for point 1. This can, however, be expected as just in the case of the tip vortices, the tip vortex and additional vortex will have an effect on each other for both tips of the wing. This influence can thus be decreased by increasing the distance between the vortices.

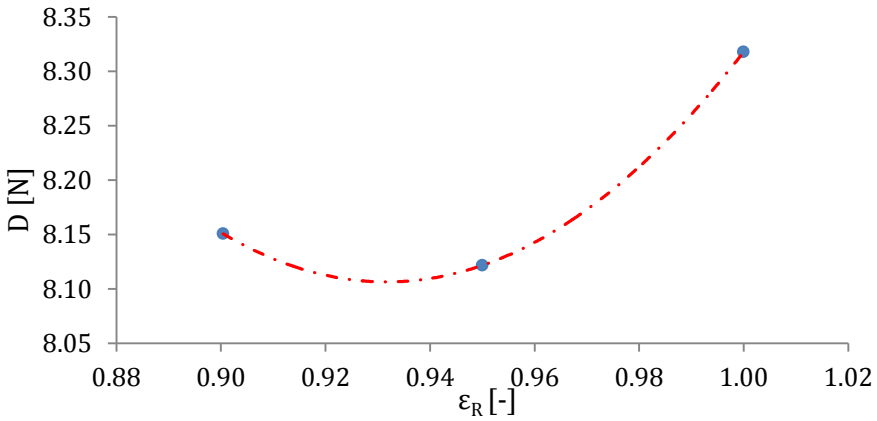

Figure 73: Elevator span ratio investigation results for point 2

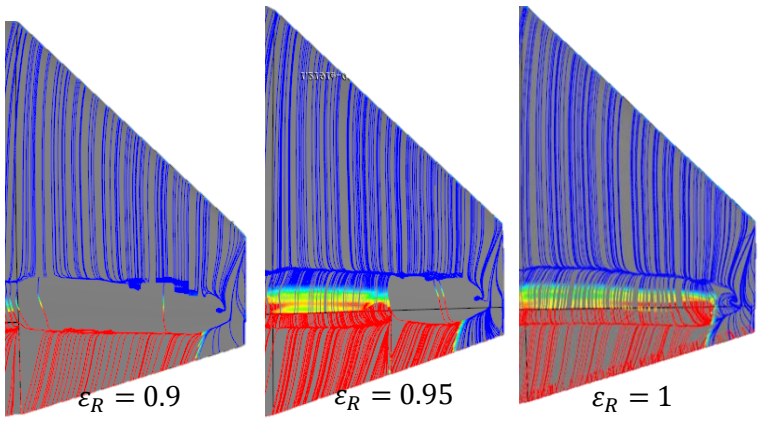

Figure 74: Tip surface flow patterns for point 2

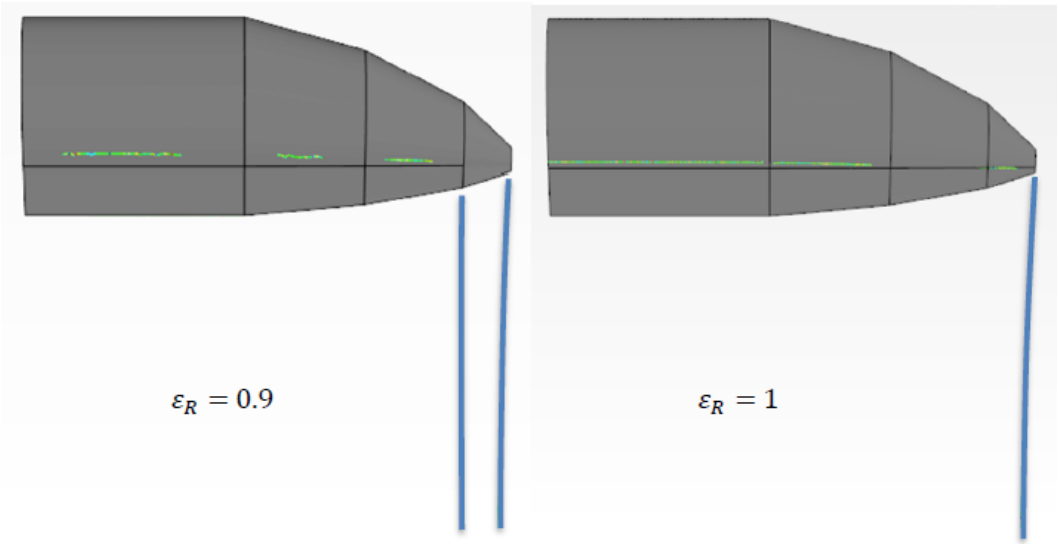

Figure 75: Vortex core locations for elevator span ratios 0.9 and 1

After consideration of both points it was decided to use the best elevator span ratio for point 1 as it represents a larger portion of the flight points due to its lower lift coefficient. An elevator span ratio of 0.97 was thus chosen as it will still give a drag reduction in point 2 compared to the planform produced by the optimisation procedure.

6.2. Tip shape

Hoerner (1965) suggested that sharp slightly upward-curved tip shapes will produce the best results. If the best elevator span ratio found in section 6.1 is

incorporated, a large portion of the tip section span will still need to be on a straight line to accommodate the elevator in the section. This results in a small section of the tip section that can be curved upwards which is not expected to give worthwhile drag reductions. It was decided to use a tip shape similar to tip shape number 6 in Figure 18. The tip section of the optimised planform was used as the baseline tip section for this investigation. Two important constraints are that the area and span of the tip section must be constant in subsequent changes. Due to this the only way to get the sharp shape is to reduce the tip chord of the tip section and incorporate curved leading and trailing edges to replace the area lost. The baseline tip section (green) and modified tip section (red) is shown in Figure 76.

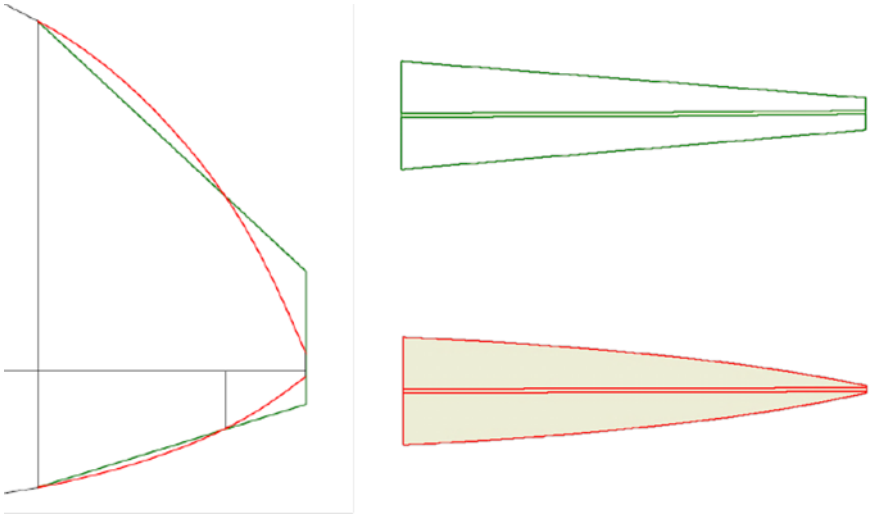

Figure 76: Optimised planform and modified tip sections

The baseline and modified tip sections where evaluated at flight points 1 and 2 with CFD. The results for flight point 1 are given in Table 16.

	Baseline tip	Hoerner tip	Difference
C_D [-]	0.005435	0.005378	-0.000057
D [N]	12.67	12.53	-0.13

Table 16: Tip shape result comparison for flight point 1

The CFD simulation for flight point 1 shows a drag reduction of 1.1% compared to the baseline tip section. The simulation results for flight point 2 are given in Table 17. A drag reduction of 3.3% is seen compared to the baseline tip section.

	Baseline tip	Hoerner tip	Difference
C_D [-]	0.012326	0.012004	-0.000322
D [N]	8.318	8.101	-0.268719

Table 17: Tip shape result comparison for flight point 2

Apart from the drag reductions seen with the elevator span ratio reduction, a slight drag reduction is also seen with the sharp tip shape. This is seen in both flight points and can be attributed to the decrease in wetted area of this section. This is further showed by skin friction plots showing high local skin friction coefficients in the region of the root chord and tip section end surface.

6.3. Summary

A new tip shape was designed for the optimised horizontal tailplane planform. Two design points were used to make design decisions. First the best elevator span ratio for the high speed point was chosen. Next a tip section shape given by Hoerner (1965) was implemented. A drag reduction of 3.3% at the low speed point was achieved together with a 1.1% drag reduction at the high speed point compared to the baseline tip section.

7. CONCLUSIONS AND RECOMMENDATIONS

7.1. Conclusions

The flight analysis procedure consisted of flight data processing and calculation of the important flight parameters needed for assessing the operating spectrum and performance of the horizontal tailplane. Calculations for a baseline horizontal tailplane showed that the total drag over a sample flight consisted of 94% profile drag and only 6% induced drag. This is due to the relatively small lift coefficients the horizontal tailplane operated at. This gives profile drag reduction priority over induced drag in the horizontal design procedure.

The planform of the new horizontal tailplane was optimised with a modified lifting line method coupled with a flight data based optimisation routine. The optimisation results show that in horizontal tailplane design the focus should firstly be on finding the minimum possible planform area which still conforms to stability requirements as this will reduce both profile and induced drag. Secondly to reduce profile drag by increasing the mean aerodynamic chord and thus the Reynolds number each section operates at. Although this was also found by Mayland (1979), up till now no clear measure of what the optimum relation between induced and profile drag for horizontal tailplanes existed. This makes flight data based optimisation especially useful in the design procedure of aerodynamic components with broad operating spectrums.

New horizontal tip section geometries were designed with the use of CFD. Two flight points were chosen to evaluate tip section performance and make design decisions. An elevator span ratio of 0.97 was chosen as it gave drag reductions in both flight points analysed and favoured the flight point more representative of the operating spectrum found through flight analysis. Small reductions in the size of the laminar separation bubbles found on the tip sections were observed together with a small increase in the vortex span due to the interaction of the tip vortex and a second trailing vortex created at the tips of the elevator. A tip section shape proposed by Hoerner (1965) was implemented. This sharp tip section shape reduced profile drag

at the tip section tips by reducing the wetted area of these areas. The vortex span was also again slightly increased resulting in a small drag reduction. Overall the tip section changes produced a 1.1% drag decrease at 149 km/h and a 3.3% decrease at 249 km/h compared to the baseline tip section.

7.2. Recommendations for further study

Multi-point aerodynamic optimisation of airfoils at two or more span-wise stations may give an extra few per cent drag reduction if this method is applied to airfoil design.

Although the optimisation routine was executed in acceptable time, further statistical reduction of flight data should be investigated to enable more sophisticated aerodynamic models to be used. Although the lifting line model was accurate it did not give flexibility to enable simultaneous airfoil, planform and tip section optimisation. Further studies can also include optimisation of the tail arm which includes a model for the added wetted area to the tail boom as the tail arm increases.

Flight data can also be used in the construction of an objective function to use in the optimisation of junction fairing on the horizontal and vertical tailplane junction and the junction between the tail boom and vertical tailplane.

References

Ákos, Z, Nagy, M, Leven, S & Vicsek, T 2010, 'Thermal Soaring Flight of Birds and UAVs', *Bioinspiration & biomimetics, 5(4),* 1-12.

Boermans, LMM & Bennis, F 1991, 'Design and Windtunnel Tests of an Airfoil for the Horizontal Tailplane of a Standard Class Sailplane', Texas.

Boermans, LLM & Waibel, G 1989, 'Aerodynamic Design of the Standard Class Sailplane ASW-24', *Technical Soaring*, July, 72-83.

Deb, K 1995, *Optimisation for Engineering Design: Algorithms and Examples*, Prentice-Hall, New Delhi.

Deperrois, A 2014, *xflr5:Analysis of Foils and Wings at Low Reynolds Numbers v6.02 Guidelines*, viewed 14 July 2014, <http://sourceforge.net/projects/xflr5/files/Guidelines.pdf>.

Drela, M & Youngren, H 2001, 'XFOIL 6.94 User Guide', Cambridge.

Eppler, R 2007, 'Airfoil Program System " PROFIL07," User's Guide'.

Fearn, RL 2008, 'Airfoil Aerodynamics Using Panel Methods', *Mathematical Journal, 10(4)*, 725-739.

Giraldo, S, Garcia, MJ & Boulanger, P 2008, 'CFD Based Wing Shape Optimization Through Gradient-Based Method', *Proceedings of the International Conference on Engineering Optimization*, Rio de Janeiro.

Glauert, H 1983, *The Elements of Airfoil and Airscrew Theory*, Cambridge University Press.

Hansen, T 2014, 'Modeling the Performance of the Standard Cirrus Glider using Navier-Stokes CFD', *Technical Soaring, 38 (1)*, 5-14.

Hicks, RM & Henne, PA 1978, 'Wing Design by Numerical Optimization', *Journal of Aircraft, 15(7)*, 407-413.

Hoerner, SF 1965, *Fluid-dynamic Drag: Practical Information on Aerodynamic Drag and Hydrodynamic Resistance*, Hoerner Fluid Dynamics, New Jersey.

Howe, D 2000, *Aircraft conceptual design synthesis*, Wiley, New York.

Lasdon, LS, Warren, AD, Jain, A & Ratner, M 1978, 'Design and testing of a generalized reduced gradient code for nonlinear programming', *ACM Transactions on Mathematical Software (TOMS) 4(1)*, 34 - 50.

Maugner, M.D. & Coder, J.G. 2010, 'Comparisons of Theoretical Methods for Predicting Airfoil Aerodynamic Characteristics'.

Mayland, K 1979, 'Optimum Tail Plane Design for Sailplanes', *Science and Technology of Low Speed and Motorless Flight*, 65-79.

Menter, FR 1994, 'Two-equation eddy-viscosity turbulence models for engineering applications', *AIAA journal 32(8)*, 1598-1605.

Neely, RH, Bollech, TV, Westrick, GC & Graham, RR 1947, 'Experimental and calculated characteristics of several NACA 44-series wings with aspect ratios of 8, 10, and 12 and taper ratios of 2.5 and 3.5', NATIONAL ADVISORY COMMITTEE FOR AERONAUTICS LANGLEY FIELD VA LANGLEY AERONAUTICAL LABORATORY.

Nelder, JA & Mead, R 1965, 'A Simplex Method for Function Minimization', *The Computer Journal ,7(4)*, 308-313.

Numec, M, Zingg, DW & Pulliam, TH 2004, 'Multipoint and Multi-Objective Aerodynamic Shape Optimization', *AIAA journal 42(6)*, 1057-1065.

Peirce, B 1852, 'Criterion for the rejection of doubtful observations', *The Astronomical Journal 2*, 161-163.

Rao, SS 2009, *Engineering Optimisation : Theory and Practice*, John Wiley & Sons, Inc., New Jersey.

Rathakrishnan, E 2013, *Theoretical Aerodynamics*, John Wiley & Sons Singapore..

Raymer, DP 1999, *Aircraft Design: A Conceptual Approach*, American Institute of Aeronautics and Astronautics, Reston, VA.

Ross, SM 2003, 'Peirce's criterion for the elimination of suspect experimental data', *Journal of Engineering Technology 20(2),* 38-41.

Selig, MS 1989, *Airfoils at Low Speeds*, H.A. Stokely, Virginia.

Silverstein, A & Katzoff, S 1939, ' Design charts for predicting downwash angles and wake characteristics behind plain and flapped wings.', NACA.

Sivells, JC & Neely, RH 1947, 'Method for Calculating Wing Characteristics by Lifting Line Theory Using Non Linear Section Lift Data', National Advisory Commitee for Aeronautics Langley Field VA Langly Aeronautical Laboratory, Hampton.

Sturdza, P 2003, 'An Aerodynamic Design Method for Supersonic Natural Laminar Flow Aircraft', Stanford University.

Tomas, F & Milgram, J 1999, *Fundamentals of Sailplane Design*, College Park Press.

van Dyke, M 1983, 'An Album of Fluid Motion', *Journal of Applied Mechanics*, p. 475.